

SPECTROSCOPY OF GRB 051111 AT $z = 1.54948$: KINEMATICS AND ELEMENTAL ABUNDANCES OF THE GRB ENVIRONMENT AND HOST GALAXY

B. E. PENPRASE¹, E. BERGER^{2,3,4}, D. B. FOX⁵, S. R. KULKARNI⁶, S. KADISH¹, L. KERBER¹,
E. OFEK⁶, M. KASLIWAL⁶, G. HILL⁷, B. SCHAEFER⁷, AND M. REED⁷

Draft version September 21, 2018

ABSTRACT

We present a high-resolution, high signal-to-noise optical spectrum of the afterglow of GRB 051111 obtained with the HIRES spectrograph on the Keck I 10-m telescope. The spectrum exhibits three redshifted absorption systems with the highest, at $z = 1.54948$, arising in the GRB host galaxy. While the Ly α feature is outside the range of our spectrum, the high column density of weakly-depleted Zn suggests that the host is a damped Ly α system with $N(\text{HI}) \gtrsim 10^{21}(Z/Z_{\odot})^{-1}$. The bulk of the gas ($> 80\%$) is confined to a narrow velocity range of $|v| < 30 \text{ km s}^{-1}$ exhibiting strong dust depletion of refractory elements such as Fe and Cr. The depletion pattern is similar to that observed in warm disk clouds of the Milky Way. We also detect absorption from all ground-level fine-structure states of Fe II, the first such example in a QSO-DLA or GRB-absorption spectrum, which indicate conditions that are consistent with the "warm disk" depletion pattern. The absorption profiles of Fe II and Mg II extend over several hundred km s^{-1} , with a depletion pattern that more closely resembles that of QSO-DLAs, suggesting that the sight line to GRB 051111 probes the halo of the host galaxy in addition to the dense disk. Thus, detailed diagnostics of the interstellar medium of GRB host galaxies continue to provide insight into regions which are generally missed in quasar surveys.

Subject headings: gamma-rays:bursts — ISM: abundances — ISM:kinematics

1. INTRODUCTION

Most of the data available for elemental abundances in the early universe come from studies of damped Ly α (DLA) systems detected in absorption against background quasars (Wolfe et al. 2005). DLAs appear to be metal poor, with a typical $Z \sim 0.03 Z_{\odot}$ (Prochaska et al. 2003), and while they exhibit evidence for star formation in a few cases, the rates typically appear to be lower than in the Lyman break galaxies at a similar redshift range (Bunker et al. 1999). Since the existence of a DLA system depends on a chance alignment of the quasar and DLA gas, and this is affected by a cross-section bias and possibly dust, it is unclear at present whether the QSO-DLAs are a representative sample of the interstellar medium within early galaxies.

An alternative approach to probing intervening gas in galaxies and the IGM is to use the afterglows of gamma-ray bursts (GRBs). In the context of the relation to star formation and the nature of DLAs, GRBs offer several advantages over quasar studies. First, GRBs are embedded in star forming galaxies with typical offsets of a few kpc or less (Bloom et al. 2002). They therefore not only provide a direct link to star formation, but also probe the regions of most intense star formation, and hence the pro-

duction and dispersal of metals. Second, since the GRB afterglow emission fades away on a timescale of days to weeks, the host galaxy and any intervening DLAs can be subsequently studied directly (e.g., Vreeswijk et al. 2004).

Third, and perhaps most important, since GRBs are likely to be located in star forming regions within their host galaxies, this approach provides the only systematic way to directly probe the small-scale environment and conditions of star formation at high redshift; the probability of intersecting an individual star-forming cloud in a quasar sight line is vanishingly small.

Over the past several years, a few absorption spectra of GRB afterglows have been obtained, revealing relatively large neutral hydrogen column densities, in some cases with $\log N(\text{HI}) > 22$ (Vreeswijk et al. 2004; Berger et al. 2005a; Chen et al. 2005). The metallicity, inferred in only a few cases, appears to be sub-solar ($Z \sim 0.01 - 0.1 Z_{\odot}$; Vreeswijk et al. 2004; Berger et al. 2005a; Chen et al. 2005; Starling et al. 2005), but with a dust-to-gas ratio that is larger than that in QSO-DLAs (Savaglio et al. 2003). In addition, some spectra reveal complex velocity structure, interpreted to arise from ordered galactic rotation (Castro et al. 2003), and in some cases appearing to arise in the complex wind environment of the progenitor star (Möller et al. 2002; Berger et al. 2005a).

¹Pomona College Department of Physics and Astronomy, 610 N. College Avenue, Claremont, CA

²Observatories of the Carnegie Institution of Washington, 813 Santa Barbara Street, Pasadena, CA 91101

³Princeton University Observatory, Peyton Hall, Ivy Lane, Princeton, NJ 08544

⁴Hubble Fellow

⁵Department of Astronomy and Astrophysics, Pennsylvania State University, 525 Davey Laboratory, University Park, PA 16802

⁶Division of Physics, Mathematics and Astronomy, 105-24, California Institute of Technology, Pasadena, CA 91125

⁷W. M. Keck Observatory, 65-1120 Mamalahoa Highway, Kamuela, HI 96743

In a continuing effort to characterize the interstellar medium of high redshift galaxies and to provide a comparison to QSO-DLAs, we present here a Keck HIRES absorption spectrum of GRB 051111, which reveals absorption from a possible DLA with a column density $\log N(\text{HI}) \gtrsim 21$ at a redshift of $z = 1.54948$. The spectrum of GRB 051111 is remarkable not only for its high resolution, which enables accurate estimates of abundances within the host galaxy, but also for the detection and accurate measurement of excited fine-structure Fe II states (Berger et al. 2005b) and a detailed examination of the kinematics within the interstellar medium of the host galaxy.

2. OBSERVATIONS

GRB 051111 was detected by *Swift* on 2005 November 11 at 06:00:02 UT. The duration of the burst is 47 s, and the fluence in the 15-150 keV band is $(3.9 \pm 0.1) \times 10^{-6}$ erg cm $^{-2}$ (H. Krimm et al. 2005). Observations with the ROTSE-IIIb robotic telescope started 27 seconds after the burst, and revealed an uncatalogued fading source located at $\alpha = 23^{\text{h}}12^{\text{m}}33.2^{\text{s}}$, $\delta = +18^{\circ}22'29.1''$ (J2000) (Rujopakarn et al. 2005).

Spectroscopic observations of GRB 051111 were initiated at 07:03 UT, approximately one hour after the burst, using the High Resolution Echelle Spectrometer (HIRES) mounted on the Keck I 10-m telescope (Hill et al. 2005). A total of 5400 s of exposure time were obtained using a $0.86''$ wide slit at airmass 1.0 – 1.2. The wavelength range covered is 4200 – 8400 Å. The spectra were reduced using the MAKEE pipeline routines (Version 4.0.1 of May 2005), which includes optimal extraction of orders, sky subtraction, and wavelength calibration from Th-Ar arc lamp exposures, including a heliocentric velocity correction. The orders within individual frames were traced using a median combined total of the exposures, and atmospheric absorption features were removed with the Makee pipeline. A final resampling of the spectrum and continuum fitting was performed using the IRAF task `continuum`. The column densities of species detected in the spectrum were computed using a set of custom-written IDL routines for measuring equivalent widths, optical depths, and for fitting curve of growth models to the detected absorption species.

The spectrum, shown in Figure 1, reveals strong absorption features at a redshift, $z_1 = 1.54948 \pm 0.00001$, which we interpret as the redshift of the host galaxy (see also Prochaska 2005⁸). In addition, we detect intervening systems at $z_2 = 1.18975$ (Mg II, Mg I, and Fe II), $z_{3a} = 0.82761$ (Mg I, Mg II, and Fe II) and $z_{3b} = 0.82698$ (Mg I and Mg II). The latter two most likely arise from the same object given their close redshifts. In addition to the GRB absorption spectrum we also obtained imaging of the GRB field with the Echelle Spectrograph and Imager on the Keck II telescope to search for host galaxy emission as discussed in §7.

3. KINEMATICS OF THE HOST GALAXY ABSORPTION LINE SYSTEM

The strongest absorption features in the spectrum of GRB 051111 arise from the redshift system $z_1 = 1.54948$, which exhibits a wide array of metal lines of Mg I, Mg II, Mn II, Cr II, Fe II, Zn II, Al III, Si II, Ni II, and the four ground-level fine-structure states of Fe II and one of Si II (Berger et al. 2005b). The line identifications, observed wavelengths, and equivalent widths (EWs) are listed in Table 1. Also included in Table 1 are estimates of the column densities based on the weak line limit for each transition using oscillator strengths and rest wavelengths from Morton (1991).

In Figures 2–14 we plot the absorption profiles for all transitions of the various ionic species as a function of velocity relative to the systemic redshift of $z_1 = 1.54948$. The majority of the lines exhibit a simple and symmetric structure extending from about -25 to $+25$ km s $^{-1}$. Lines of Fe II and Mg II exhibit in addition to the narrow component absorbers in the range of -150 to $+50$ km s $^{-1}$ and -250 to $+170$ km s $^{-1}$, respectively. The absorption lines of Al III and Si II exhibit an intermediate kinematic structure with only a negative velocity extension.

The relatively low redshift precludes a direct detection of the Ly α line within the wavelength range of our spectrum, but most likely this system resembles a DLA in its neutral hydrogen column density. In the discussion below we provide an estimate of the approximate column density of neutral hydrogen by scaling the column of weakly-depleted Zn along with the average metallicity of QSO-DLAs at a similar redshift range.

The different line profiles can be interpreted to arise from physical features in the host galaxy in the following way. First, the detection of positive velocity structure in Fe II and Mg II suggests that the burst was located on the far side of the host galaxy such that the disk and/or halo rotation are traced in both negative and positive velocity. The much larger extension at negative velocity is expected since the burst is embedded in the disk and does not trace its full extent on the far side. The velocity range of $|v| \lesssim 250$ km s $^{-1}$ is typical of the high velocity and halo gas within our galaxy (Albert et al. 1993) and matches a range of velocities for quasar absorption line systems known to probe galaxy halos (Ellison et al. 2003). It is possible that some of the higher velocity absorption may arise from infall and/or outflow of metal enriched gas. However, this interpretation is difficult to reconcile with the narrowness of the positive and negative velocity features (Figures 2 and 8), which show line widths of $b \approx 10$ km s $^{-1}$.

On the other hand, the main absorption component centered on zero velocity is physically co-located with the burst, based on its unusual properties as derived below, and the possibility that it is actually influenced by the burst (Berger et al. 2005b). We show that this region is unlike any that have been found in quasar spectra, but it is generally similar to absorbers in other GRB spectra. This suggests a fairly compact region with a cross-section that is too small to be probed in quasar sight lines, most likely a molecular cloud or an individual star-forming region.

⁸A GRB Coordinates Network (GCN) Circular by Prochaska (2005) provides a cursory list of some properties of the host galaxy absorption system.

4. ELEMENTAL ABUNDANCES WITHIN THE HOST GALAXY OF GRB 051111

We employ multiple techniques to investigate in detail the abundance patterns of the narrow component centered at $v = 0 \text{ km s}^{-1}$, and those of the extended positive and negative velocity structures. Since some of the absorption features are saturated we make use of a curve-of-growth (COG) analysis (Spitzer 1978), which allows us to correlate the equivalent widths

$$W_\lambda = \frac{2bF(\tau_0)\lambda}{c}, \quad (1)$$

with the line center's optical depth given by

$$\tau_0 = \frac{\pi^{1/2}e^2 f_\lambda \lambda N}{m_e c b} = 1.496 \times 10^{-15} \frac{f_\lambda (\lambda/\text{\AA}) N}{(b/\text{km s}^{-1})}, \quad (2)$$

using the function

$$F(\tau_0) = \int_0^\infty [1 - \exp(-\tau_0 e^{-x^2})] dx. \quad (3)$$

Here f_λ is the oscillator strength, W_λ is the equivalent width, λ is the rest wavelength, and we assume that all species share the same value of the Doppler parameter, b . We fit iteratively for b and the column density of each species (e.g., Savaglio et al. 2003). The resulting best-fit COG, with a Doppler parameter, $b \approx 10 \text{ km s}^{-1}$, is shown in Figure 15, and the column densities are listed in Table 2.

From the combined COG analysis we note that the best fit value of $b = 10 \text{ km s}^{-1}$ is comparable to the observed values of Ca II line widths for atomic filaments and translucent molecular clouds in our galaxy (e.g., Penprase & Blades 2000; Penprase 1993), as well as for the well-studied sight lines of Zeta Oph, for which HST observations of ions ranging from Mg II to Zn II show absorption over a velocity range of 20 km s^{-1} , and structure with typical widths of approximately $5 - 10 \text{ km s}^{-1}$ (Savage & Sembach 1996).

To obtain additional information on the column density velocity structure, $N(v)$, and the abundances of elements as a function of velocity, we also use the apparent optical depth method (Savage & Sembach 1991) where

$$N = \int N(v) dv = \frac{m_e c}{\pi e^2 f_\lambda} \int \tau(v) dv, \quad (4)$$

and the optical depth

$$\tau(v) = \ln[I_0(v)/I(v)]. \quad (5)$$

This method has the advantage that it makes no *a priori* assumptions about the functional form of the velocity distribution, and at the same time it incorporates information from a wide variety of lines with different oscillator strengths. By combining the optical depths of these lines, and eliminating the contribution from high optical depth and saturated velocity channels in the coadded velocity spectrum, an improved estimate of both the column density and the velocity structure of the line profile is obtained, which include a measurement of the velocity structure within the cores of the lines.

We apply the apparent optical depth technique to all of the detected absorbing species and summarize the resulting column densities in Table 2; the $N(v)$ profiles are shown in Figures 16–18. We also include in Table 2 the adopted column density for each species which is either derived from the apparent optical depth approach or an average with the COG values, depending on the number of transitions, and degree of saturation. Based on the shapes of the various lines we define three velocity ranges — z_{1a} : $v < -30 \text{ km s}^{-1}$, z_{1b} : $-30 < v < +30 \text{ km s}^{-1}$, and z_{1c} : $v > +30 \text{ km s}^{-1}$ — and determine the column densities in each range. This is particularly useful for the Fe II and Mg II which exhibit a wide velocity range. We find that the dominant z_{1b} system accounts for about 85% of the Fe II column and $\gtrsim 70\%$ of the Mg II column.

We estimate the neutral hydrogen column density using the column density of Zn II since Zn is a non-refractory iron peak element and its gas-phase abundance should therefore closely match the gas metallicity. Based on a value of $\log N(\text{ZnII}) = 13.58 \pm 0.15$ and a typical metallicity of $[\text{Zn}/\text{H}] \approx -1$ for DLAs at $z \sim z_1$ (Akerman et al. 2005), we derive $\log N(\text{HI}) \approx 21.9$, indicating a DLA with an H I column density that is similar to those of some other GRB absorption systems (e.g., Vreeswijk et al. 2004; Berger et al. 2005a), and is significantly larger than in typical QSO-DLAs. This is not surprising since the Zn II column density exceeds the highest column densities measured in QSO-DLAs by about 0.5 dex, and the median value by nearly 1.5 dex (Figure 19). As we show below, the detailed abundance pattern of the main absorption component (z_{1b}) is markedly different than in QSO-DLAs and along with the large inferred value of $N(\text{HI})$ reflects the fact that it is a region of the ISM that is generally missed in quasar sight lines.

5. DEPLETION PATTERNS AND DUST WITHIN THE GRB 051111 HOST GALAXY

The difference in the velocity structure of various species, coupled with the expected difference in depletion for the non-refractory (e.g., Zn) and refractory (e.g., Fe) elements, indicates that the sight line to GRB 051111 likely probes various components of the host galaxy's interstellar medium. We begin by investigating the main absorption component z_{1b} . The column density ratios of various species compared to the non-refractory Zn II are shown in Figure 20, along with the values for past GRB-DLAs and for QSO-DLAs in Figure 19.

We find that for z_{1b} the Cr to Zn ratio is $[\text{Cr}/\text{Zn}] = -0.8 \pm 0.2$, which is at the low end of the distribution for QSO-DLAs with $\langle [\text{Cr}/\text{Zn}] \rangle = -0.3 \pm 0.3$ (Figure 19). Since Cr and Zn are produced in the same nucleosynthetic pathway, differences in the abundances of these elements arise from differential dust depletion. Similarly, the ratio $[\text{Fe}/\text{Zn}] = -1.3 \pm 0.2$ is significantly lower than in QSO-DLAs for which $\langle [\text{Fe}/\text{Zn}] \rangle = -0.5 \pm 0.3$. We find the same results for the ratios of Si and Mn relative to Zn. In all cases our elemental abundances are referenced relative to the Solar values in Lodders (2003). Taken in conjunction with the unusually large Zn II column density compared to QSO-DLAs, we conclude that the main absorption component is dense and strongly dust-depleted.

The large Zn II column density and strong depletion are remarkably similar to those measured in past GRB absorption systems (Savaglio & Fall 2004). This suggests that GRB sight lines probe similar regions at various redshifts reflecting a possible uniformity in the environmental conditions that support GRB progenitor formation and possibly star formation in general. Similarly, the strong dust depletion indicates that similar regions are missed in quasar sight lines not just because of their small cross-section, but also because of the associated dust extinction.

Given that Zn is largely undepleted, we estimate the dust content along the sight line to GRB 051111 to be about 2.5 times higher than in typical DLA gas, but comparable, per unit metallicity, to Milky Way gas. Applying our adopted metallicity of 1/10 solar we find that the dust-to-gas ratio is approximately 1/12 that of Milky Way gas, scaling the relation described in Pettini (2004). With our estimated column density of $\log N(\text{HI}) \approx 21.9$, we then expect about 0.55 magnitudes of V -band extinction toward GRB 051111 using the relation $\langle N(\text{HI})/A_V \rangle = 1.5 \times 10^{21} \text{ cm}^{-2} \text{ mag}^{-1}$ (Diplas & Savage 1994). Using an SMC extinction curve appropriate for low-metallicity gas (Bouchet et al. 1985), we derive that the GRB 051111 sight line has an extinction of $A(1500) \sim 2.5$ magnitudes in the rest frame UV.

As described in detail in Savage & Sembach (1996), depletion patterns can reveal the presence of warm and cold gas along the line of sight. The full depletion pattern for the z_{1b} component is shown in Figure 20 in comparison to the four typical patterns observed in the Milky Way of warm halo (WH), warm disk+halo (WDH), warm disk (WD), and cool disk (CD) clouds (Savage & Sembach 1996). We note that the Mg absorption lines are heavily saturated and the inferred abundance is therefore a lower limit. Similarly, in the case of Al, only the Al III transition is observed, and we are therefore unable to account for any additional Al II gas. Taking these effects into account we find that the observed abundances closely match the WD pattern, or marginally the WDH pattern. The more weakly depleted WH and the strongly-depleted CD do not provide an adequate fit to the data.

So far we have discussed only the main component of the line absorption profiles, but it is clear from the different shape of the Fe II and Mg II lines compared to the other species that the depletion pattern changes across the line profile. We find that $[\text{Fe}/\text{Zn}] > -1.9$ (z_{1a}) and $[\text{Fe}/\text{Zn}] > -1.2$ (z_{1c}), along with the limits of $\log N(\text{ZnII}) \lesssim 12.7$ are similar to those found in QSO-DLAs (Figure 19), but are different from the depleted z_{1b} component. This suggests that the sight line to GRB 051111 probes in addition to the dense component in the GRB local environment, a region in the halo of the host galaxy, which is typical of the sight lines probed by background quasars. Given the combination of kinematic structure and abundance patterns we find that the GRB probably exploded away from the center of the galaxy, most likely in the spiral arm of a highly inclined disk.

6. FINE-STRUCTURE EXCITATION OF FE II AND SI II

In addition to the various transitions discussed above, from which we deduce a warm and depleted environment in the z_{1b} absorber co-located with the GRB, we also detect absorption lines arising from all of the available ground-level fine-structure states of Fe II and Si II. A detailed analysis of these lines and the inferred physical conditions are summarized in a companion paper (Berger et al. 2005b), but we investigate this here in the context of the inferred depletion pattern.

As shown in Figure 17, the velocity structure of the Fe II fine-structure levels is similar to that of the dense and depleted component, z_{1b} . The Si II* transition is weaker and as a result the velocity structure is not clear, but the strongest absorption arises from $v \approx 0 \text{ km s}^{-1}$ (Figure 17). We use the apparent optical depth method over the full velocity range of $|v| < 30 \text{ km s}^{-1}$ to derive the column densities of the fine-structure states (see Table 2). We find that $\log N(\text{SiII}^*) = 14.96$ is somewhat higher than the column densities measured in GRB 050505 ($\log N \approx 14.7$; Berger et al. 2005a), GRB 030323 ($\log N \approx 14.2$; Vreeswijk et al. 2004), and GRB 020813 ($\log N \approx 14.3$; Savaglio & Fall 2004).

The excitation of the fine-structure levels requires either a combination of a high temperature and a high gas volume density, or an intense IR or UV radiation field. As we show in Berger et al. (2005b), the radiation field may be due to the GRB itself, but in the case of excitation by the ambient radiation field due to star formation activity, the inferred luminosity and size of the region would naturally lead to a warm, dust-depleted environment.

In particular, excitation of the fine-structure levels by an IR radiation field, along with the observed ratios of the Fe II and Si II fine-structure levels, are indicative of a warm dust spectrum, $F_\nu \propto \nu^{2.2}$ with $T \gtrsim 600 \text{ K}$. The alternative interpretation of collisional excitation similarly leads to a large electron volume density, $n_e \gtrsim 10^3 \text{ cm}^{-3}$, and temperature, $T_e \sim 10^3 \text{ K}$ (Figure 21). In both scenarios we expect that the depletion pattern would be similar to that of a warm disk environment, and with a significant depletion.

7. GRB HOST GALAXY IMAGING

In an attempt to place the information from the absorption spectrum of GRB 051111 in the overall context of the host galaxy properties, we observed the position of the burst with the Echelle Spectrograph and Imager (ESI) mounted on the Keck II telescope on 2005 November 30. A total of 1500 s were obtained in R -band. At the position of the afterglow we detect a faint extended source which we identify as the host galaxy (Figure 22). A comparison to two nearby and unsaturated stars in the USNO-B catalog indicates a brightness of $R = 26 \pm 0.3 \text{ mag}$ for this object. At the redshift z_1 and assuming a spectrum $F_\nu \propto \nu^{-1}$, this translates to an absolute rest-frame B -band magnitude of about -18.6 or $L \approx 0.1 L^*$. This value is similar to that of other GRB host galaxies which at a similar redshift range from about -17 to -21 mag .

Since the observed R -band probes the rest-frame UV emission from the host galaxy, we can roughly estimate the star formation rate in the host galaxy. Using the re-

lation of Kennicutt (1998), $\text{SFR} = 1.4 \times 10^{-28} L_\nu$, we find that $\text{SFR} \approx 3 M_\odot \text{ yr}^{-1}$. Clearly, this value is subject to a large upward correction due to possible dust extinction. If the estimated extinction provided above based on the depletion pattern in the GRB local environment is representative, then it is possible that the star formation rate easily exceeds $30 M_\odot \text{ yr}^{-1}$.

8. INTERVENING SYSTEMS

Within the spectrum of GRB 051111 we detect intervening absorption systems at $z_2 = 1.18975$ from absorption by Mg II, Mg I, and Fe II. The column densities for these systems derived from optical depth and COG fitting of the absorption lines are $\log N(\text{MgII}) = 14.33 \pm 0.05$, $\log N(\text{MgI}) = 12.58 \pm 0.1$, and $\log N(\text{FeII}) = 14.31 \pm 0.05$. An additional pair of absorption systems are seen at $z_{3a} = 0.82761$ and $z_{3b} = 0.82698$ in the species Mg I, Mg II, and Fe II. For the absorption system at $z_{3a} = 0.82761$, we estimate column densities of $\log N(\text{MgII}) = 13.28 \pm 0.1$, $\log N(\text{MgI}) = 12.38 \pm 0.1$, and $\log N(\text{FeII}) = 12.95 \pm 0.05$. The column densities of the absorption lines at $z_{3b} = 0.82698$ are $\log N(\text{MgII}) = 13.1 \pm 0.15$, and $\log N(\text{FeII}) = 12.70 \pm 0.05$.

Bowen et al. (1995) conducted a survey of Mg II absorption from the disks and halos of 17 low-redshift galaxies, and studied the correlation between the impact parameter, ρ , and the line equivalent width. The sample includes a range of $\rho \approx 2 - 113$ kpc, and equivalent widths from 0.05 to 2 Å. Systems with Mg II equivalent widths $> 0.1\text{Å}$ appear to have smaller impact parameters, $\rho < 20 - 30$ kpc, while the largest impact parameter systems are seen to have much smaller equivalent widths. The z_2 and z_3 intervening systems in the spectrum of GRB 051111 exhibit equivalent widths of 1.7Å and 0.2Å, respectively. Thus, both of these intervening systems are at the high end of the Bowen et al. (1995) sample, indicating small impact parameters.

Our image of the field of GRB 051111 reveals two nearby galaxies, which are significantly brighter than the GRB host, one located 2'' to the north and the other about 2.5'' to the west (Figure 22). While we do not have redshifts for these galaxies, it is likely that they are responsible for the intervening systems z_2 and z_{3ab} . The derived impact parameters relative to the GRB position are about 17 and 20 kpc, indicating that the intervening absorbers are similar to those found by Bowen et al. (1995).

9. DISCUSSION AND CONCLUSIONS

The high resolution spectrum of GRB 051111 reveals a range of interstellar abundance patterns within the host

galaxy. In addition to warm halo gas which is typical of quasar sight lines and which represents the bulk of the galaxy cross-section, we detect a high column density, kinematically cold region of dust-depleted gas, which is typical of a warm disk abundance pattern. The observed abundance pattern in this component is similar to those in several other GRB absorption spectra obtained in the past. The weaker Fe and Mg absorption with a wider positive and negative velocity extension of several hundred km s^{-1} suggests that the GRB location was offset from the center of the galaxy. While the Ly α line is not detected in our spectrum, a reasonable value of the metallicity $Z \sim 0.1 Z_\odot$, combined with a large Zn II abundance indicates that the host is likely a DLA with $\log N(\text{HI}) \approx 21.9$, higher than typical QSO-DLAs but in good agreement with other GRB-DLA systems (Vreeswijk et al. 2004; Berger et al. 2005a; Chen et al. 2005).

The detection of strong absorption from Fe II and Si II fine-structure levels (discussed in detail in Berger et al. 2005b) requires physical conditions that are in good agreement with the conclusion that the local environment is warm and dust-depleted. In the case of collisional excitation the inferred temperature is about 10^3 K, while in the case of IR pumping dust re-processing is probably essential for generating the required IR radiation field.

We finally identify the host galaxy and the likely counterparts of the two intervening systems detected in the spectrum. As in the case of previous GRB hosts, the galaxy is relatively faint, $L \sim 0.1 L^*$. A comparison of the Mg II column densities of the intervening systems with the offsets of the two nearby galaxies relative to the GRB position is in good agreement with previous correlations with impact parameters found in the context of quasar studies. If the intervening systems occurred at a higher redshift in which we could determine directly whether they are DLAs, one can imagine that similar imaging, as well as follow-up spectroscopy, would provide direct insight into the nature of DLAs, a question that remains difficult to address in the context of QSO-DLAs.

BEP would like to thank Pomona College for support from a Downing Exchange fellowship to Cambridge University, and would like to thank Max Pettini, Edward Jenkins, and Bruce Draine for helpful discussions. EB is supported by NASA through Hubble Fellowship grant HST-01171.01 awarded by the Space Telescope Science Institute, which is operated by AURA, Inc., for NASA under contract NAS 5-26555.

References

- Akerman, C. J., Ellison, S. L., Pettini, M., & Steidel, C. C. 2005, *A&A*, 440, 499
- Albert, C. E., Blades, J. C., Morton, D. C., Lockman, F. J., Proulx, M., & Ferrarese, L. 1993, *ApJS*, 88, 81
- Berger, E., Penprase, B. E., Cenko, S. B., Kulkarni, S. R., Fox, D. B., Steidel, C. C., & Reddy, N. A. 2005a, *ArXiv Astrophysics e-prints*
- Berger, E., Penprase, B. E., Fox, D. B., Kulkarni, S. R., Hill, G., Schaefer, B., & Reed, M. 2005b, *ArXiv Astrophysics e-prints*

- Bloom, J. S., Kulkarni, S. R., & Djorgovski, S. G. 2002, *AJ*, 123, 1111
- Bouchet, P., Lequeux, J., Maurice, E., Prevot, L., & Prevot-Burnichon, M. L. 1985, *A&A*, 149, 330
- Bowen, D. V., Blades, J. C., & Pettini, M. 1995, *ApJ*, 448, 634
- Bunker, A. J., Warren, S. J., Clements, D. L., Williger, G. M., & Hewett, P. C. 1999, *MNRAS*, 309, 875
- Castro, S., Galama, T. J., Harrison, F. A., Holtzman, J. A., Bloom, J. S., Djorgovski, S. G., & Kulkarni, S. R. 2003, *ApJ*, 586, 128
- Chen, H.-W., Prochaska, J. X., Bloom, J. S., & Thompson, I. B. 2005, *ArXiv Astrophysics e-prints*
- Diplas, A., & Savage, B. D. 1994, *ApJ*, 427, 274
- Ellison, S. L., Mallén-Ornelas, G., & Sawicki, M. 2003, *ApJ*, 589, 709
- H. Krimm, H., et al. 2005, *GRB Circular Network*, 4260, 1
- Hill, G., Prochaska, J. X., Fox, D., Schaefer, B., & Reed, M. 2005, *GRB Circular Network*, 4255, 1
- Keenan, F. P., Hibbert, A., Burke, P. G., & Berrington, K. A. 1988, *ApJ*, 332, 539
- Kennicutt, R. C. 1998, *ARA&A*, 36, 189
- Lodders, K. 2003, *ApJ*, 591, 1220
- Möller, P., et al. 2002, *A&A*, 396, L21
- Morton, D. C. 1991, *ApJS*, 77, 119
- Penprase, B. E. 1993, *ApJS*, 88, 433
- Penprase, B. E., & Blades, J. C. 2000, *ApJ*, 535, 293
- Pettini, M. 2004, in *Cosmochemistry. The melting pot of the elements*, 257
- Prochaska, J. X. 2005, *GRB Circular Network*, 4271, 1
- Prochaska, J. X., Gawiser, E., Wolfe, A. M., Cooke, J., & Gelino, D. 2003, *ApJS*, 147, 227
- Rujopakarn, W., Swan, H., Rykoff, E. S., & Schaefer, B. 2005, *GRB Circular Network*, 4247, 1
- Savage, B. D., & Sembach, K. R. 1991, *ApJ*, 379, 245
- Savage, B. D., & Sembach, K. R. 1996, *ARA&A*, 34, 279
- Savaglio, S., & Fall, S. M. 2004, *ApJ*, 614, 293
- Savaglio, S., Fall, S. M., & Fiore, F. 2003, *ApJ*, 585, 638
- Spitzer, L. 1978, *Physical processes in the interstellar medium* (New York Wiley-Interscience, 1978. 333 p.)
- Starling, R. L. C., et al. 2005, *A&A*, 442, L21
- Vreeswijk, P. M., et al. 2004, *A&A*, 419, 927
- Wolfe, A. M., Gawiser, E., & Prochaska, J. X. 2005, *ARA&A*, 43, 861

TABLE 1
LINE IDENTIFICATION

λ_{obs} (Å)	Line (Å)	f_{ij}	z	W_0 (Å)	$\log N$ (cm^{-2})
4353.26	Fe II 2382.7650	0.32000	0.82698	0.09582	12.58
4354.79	Fe II 2382.7650	0.32000	0.82762	0.13127	12.78
4358.60	Ni II 1709.6042	0.03240	1.54948	0.09561	13.76
4440.05	Ni II 1741.5531	0.04270	1.54948	0.09213	13.64
4455.97	Mg I 1747.7937	0.00934	1.54948	0.09585	14.36
4466.47	Ni II 1751.9157	0.02770	1.54948	0.08595	13.75
4607.70	S I 1807.3113	0.11050	1.54948	0.07275	13.09
4609.49	Si II 1808.0130	0.00219	1.54948	0.22796	15.77
4632.22	Si II* 1816.9285	0.00166	1.54948	0.03723	14.55
4660.28	Mg I 1827.9351	0.02450	1.54948	0.13838	14.29
4707.90	Mn II 2576.8770	0.35080	0.82698	0.01619	11.72
4709.55	Mn II 2576.8770	0.35080	0.82762	0.03428	12.02
4728.56	Al III 1854.7164	0.53900	1.54948	0.19586	12.97
4741.76	Mn II 2594.4990	0.27100	0.82762	0.02474	11.98
4749.14	Al III 1862.7895	0.26800	1.54948	0.13177	12.96
4750.46	Fe II 2600.1730	0.22390	0.82698	0.04929	12.37
4752.13	Fe II 2600.1730	0.22390	0.82762	0.10517	12.76
5108.88	Mg II 2796.3520	0.61230	0.82698	0.14426	12.43
5110.67	Mg II 2796.3520	0.61230	0.82762	0.22484	12.83
5122.00	Mg II 2803.5310	0.30540	0.82698	0.11927	12.64
5123.79	Mg II 2803.5310	0.30540	0.82762	0.19326	13.07
5133.24	Fe II 2344.2140	0.11400	1.18975	0.71346	14.09
5165.59	Zn II 2026.1360	0.48900	1.54948	0.19034	13.19
5214.13	Mg I 2852.9640	1.83000	0.82762	0.19037	12.12
5217.66	Fe II 2382.7650	0.32000	1.18975	1.11235	13.99
5242.38	Cr II 2056.2539	0.10500	1.54948	0.14935	13.46
5258.72	Zn II 2062.6640	0.25600	1.54948	0.17199	13.24
5267.64	Cr II 2066.1610	0.05150	1.54948	0.09474	13.42
5693.73	Fe II 2600.1730	0.22390	1.18975	1.23064	14.01
5736.02	Fe II 2249.8768	0.00182	1.54948	0.09490	14.80
5763.81	Fe II 2260.7805	0.00244	1.54948	0.13672	14.87
5935.47	Fe II** 2328.1112	0.03450	1.54948	0.07175	13.30
5949.25	Fe II* 2333.5156	0.07780	1.54948	0.15565	13.41
5962.53	Fe II*** 2338.7248	0.08970	1.54948	0.10608	13.08
5976.53	Fe II 2344.2140	0.11400	1.54948	0.37211	14.05
5978.53	Fe II**** 2345.0011	0.15300	1.54948	0.10861	12.84
6016.33	Fe II*** 2359.8278	0.06790	1.54948	0.07552	13.03
6030.93	Fe II* 2365.5518	0.04950	1.54948	0.13941	13.49
6053.64	Fe II 2374.4612	0.03130	1.54948	0.29999	14.43
6074.81	Fe II 2382.7650	0.32000	1.54948	0.41259	13.59
6091.62	Fe II* 2389.3582	0.08250	1.54948	0.19033	13.50
6109.46	Fe II* 2396.3559	0.31619	1.54948	0.28800	13.37
6123.31	Mg II 2796.3520	0.61230	1.18975	1.99290	13.93
6131.92	Fe II*** 2405.1638	0.02600	1.54948	0.05041	13.22
6133.08	Fe II** 2405.6186	0.23700	1.54948	0.25156	13.31
6139.03	Mg II 2803.5310	0.30540	1.18975	1.68043	14.13
6147.44	Fe II*** 2411.2533	0.21000	1.54948	0.18791	13.04
6148.84	Fe II**** 2411.8023	0.21000	1.54948	0.10497	12.68
6154.56	Fe II**** 2414.0450	0.17500	1.54948	0.10723	12.77
6247.28	Mg I 2852.9640	1.83000	1.18975	0.38539	12.24
6569.70	Mn II 2576.8770	0.35080	1.54948	0.23663	13.08
6594.61	Fe II 2586.6500	0.36933	1.54948	0.06840	14.09
6614.62	Mn II 2594.4990	0.27100	1.54948	0.22355	13.23
6629.09	Fe II 2600.1730	0.22390	1.54948	0.44168	13.75
6648.70	Fe II** 2607.8664	0.11800	1.54948	0.20213	13.28
6660.91	Fe II* 2612.6542	0.12600	1.54948	0.25575	13.50
6675.56	Fe II** 2618.3991	0.05050	1.54948	0.10022	13.22
6685.89	Fe II**** 2622.4518	0.05600	1.54948	0.04794	12.79
6696.08	Fe II* 2626.4511	0.04410	1.54948	0.15064	13.50
6702.78	Fe II**** 2629.0777	0.17300	1.54948	0.12269	12.76
6710.51	Fe II** 2632.1081	0.22860	1.54948	0.08600	13.40
7129.24	Mg II 2796.3520	0.61230	1.54948	0.55706	13.41
7147.55	Mg II 2803.5310	0.30540	1.54948	0.55682	13.70

NOTE.—Absorption features identified in the spectrum of GRB 051111. The columns are (left to right): (i) Observed wavelength, (ii) line identification, (iii) oscillator strength, (iv) redshift of the line, (v) rest-frame equivalent width, and (vi) logarithm of the column density assuming the optically-thin case; in most cases this is a lower limit since the lines are generally saturated.

TABLE 2
COLUMN DENSITIES OF IONS IN z_1

Ion	COG			AOD			Adopted		
	z_{1a}	z_{1b}	z_{1c}	z_{1a}	z_{1b}	z_{1c}	z_{1a}	z_{1b}	z_{1c}
Mg II	15.05	> 14.78	13.59	14.22	> 13.88	13.62	14.22 ± 0.08	> 14.70	13.62 ± 0.08
Mg I	< 13.6	14.85	< 13.4	< 13.26	14.72	< 13.1	< 13.3	14.72 ± 0.01	< 13.1
Al III	< 13.2	13.39	< 12.4	13.05	13.34	< 12.4	13.05 ± 0.20	13.34 ± 0.10	< 12.4
Si II	14.13	16.18	< 14.5	14.13 ± 0.10	16.18 ± 0.20	< 14.5
Si II*	< 14.1	14.96	< 14.5	< 14.1	14.96 ± 0.02	< 14.5
S I	< 12.3	13.50	< 12.6	< 12.3	13.50 ± 0.02	< 12.6
Cr II	< 13.2	13.80	< 11.8	< 12.9	13.85	< 11.9	< 12.9	13.85 ± 0.10	< 11.9
Mn II	< 10.4	13.84	< 11.5	< 10.4	13.52	< 11.6	< 10.4	13.52 ± 0.15	< 11.6
Fe II	14.66	15.32	14.51	14.29	15.15	13.74	14.29 ± 0.10	15.15 ± 0.10	13.74 ± 0.10
Fe II*	< 12.5	13.91	...	< 12.2	13.90	< 12.3	< 12.2	13.90 ± 0.10	< 12.3
Fe II**	< 12.5	13.70	< 12.2	< 12.2	13.70	< 12.0	< 12.2	13.70 ± 0.08	< 12.0
Fe II***	< 12.5	13.54	< 12.1	< 12.2	13.52	< 12.1	< 12.2	13.53 ± 0.10	< 12.1
Fe II****	< 12.8	13.21	< 12.0	< 12.5	13.15	< 12.0	< 12.5	13.18 ± 0.10	< 12.1
Ni II	< 13.5	15.05	< 12.9	< 14.2	13.99	< 12.8	< 13.5	13.99 ± 0.35	< 12.8
Zn II	< 11.7	13.87	< 11.9	< 11.8	13.58	< 12.0	< 11.8	13.58 ± 0.15	< 12.0

NOTE.—Ionic column densities and abundances as derived from the curve-of-growth analysis and apparent optical depth technique. The three velocity ranges are defined in §4.

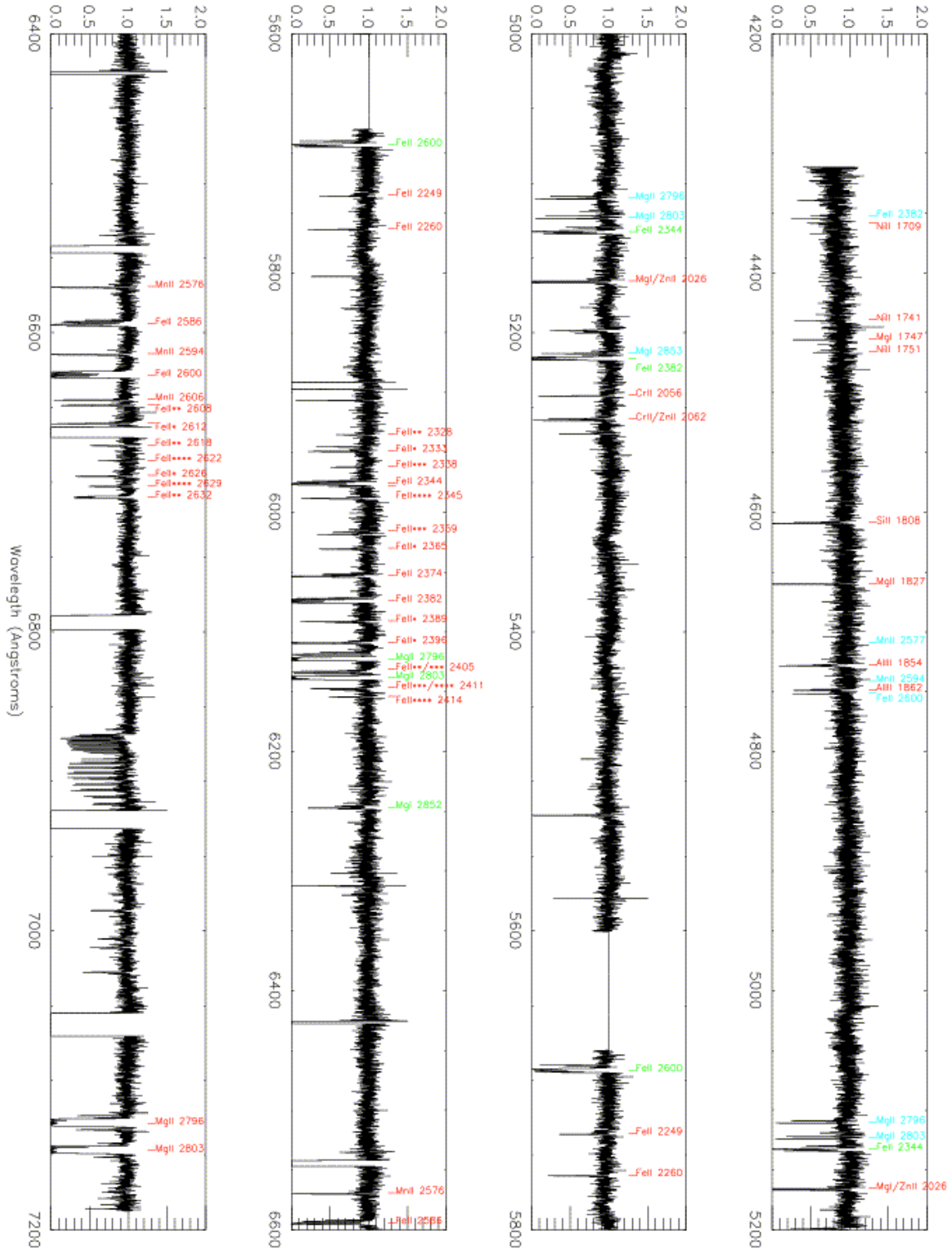


FIG. 1.— Complete spectrum of GRB 051111 obtained with HIRES on the Keck I telescope showing the spectrum of chips 1 and 2, which spans wavelengths from 4300 to 7200 Å. Absorption lines from the system at $z_1 = 1.54958$ are indicated in red, while features from the system at $z_2 = 1.18975$ are indicated in green and those from $z_{3ab} = 0.827$ are shown in blue.

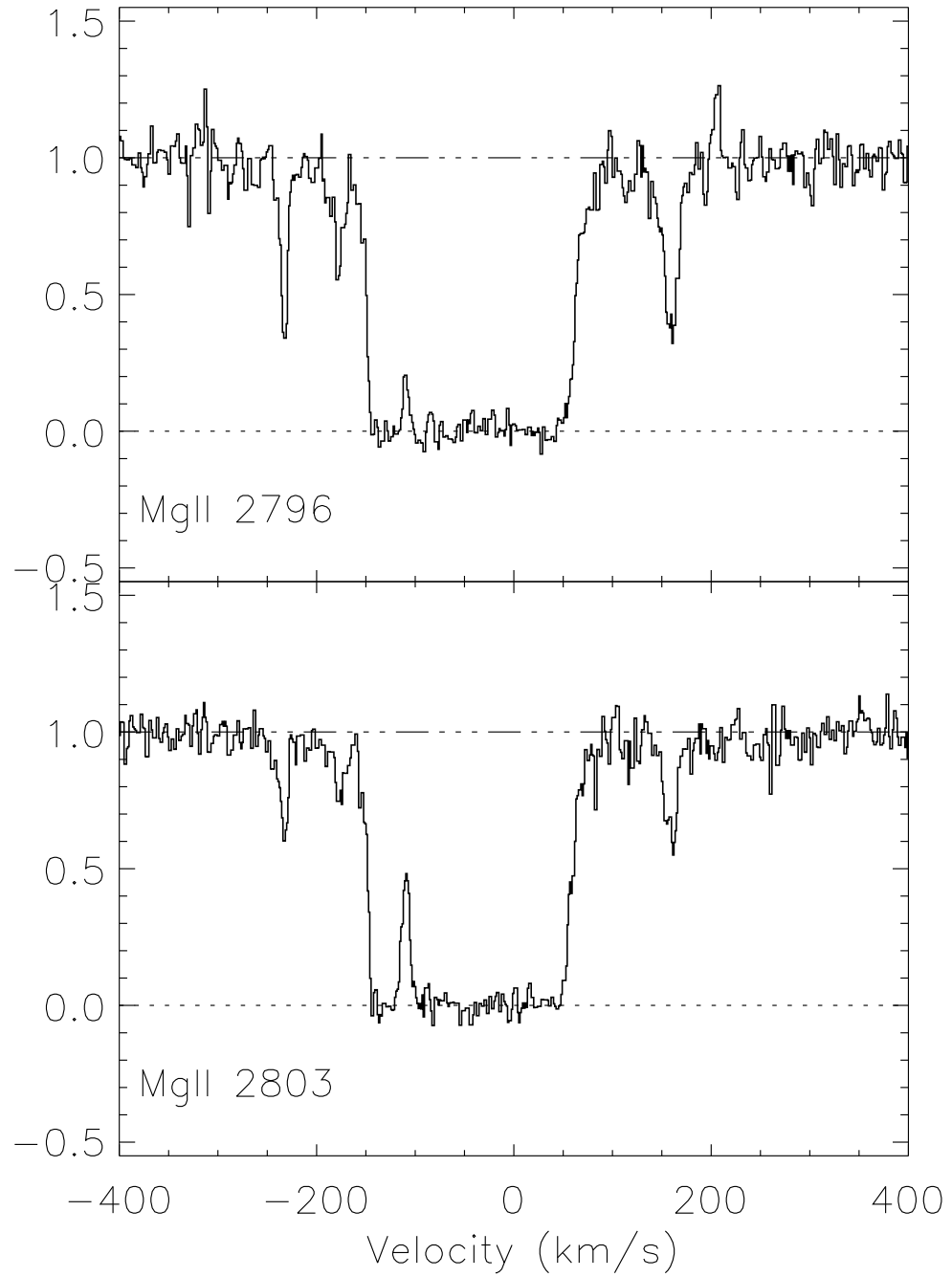


FIG. 2.— Spectrum of Mg II absorption within host galaxy of GRB 051111 in the rest frame of $z_1 = 1.54948$. Observational details are given in §2.

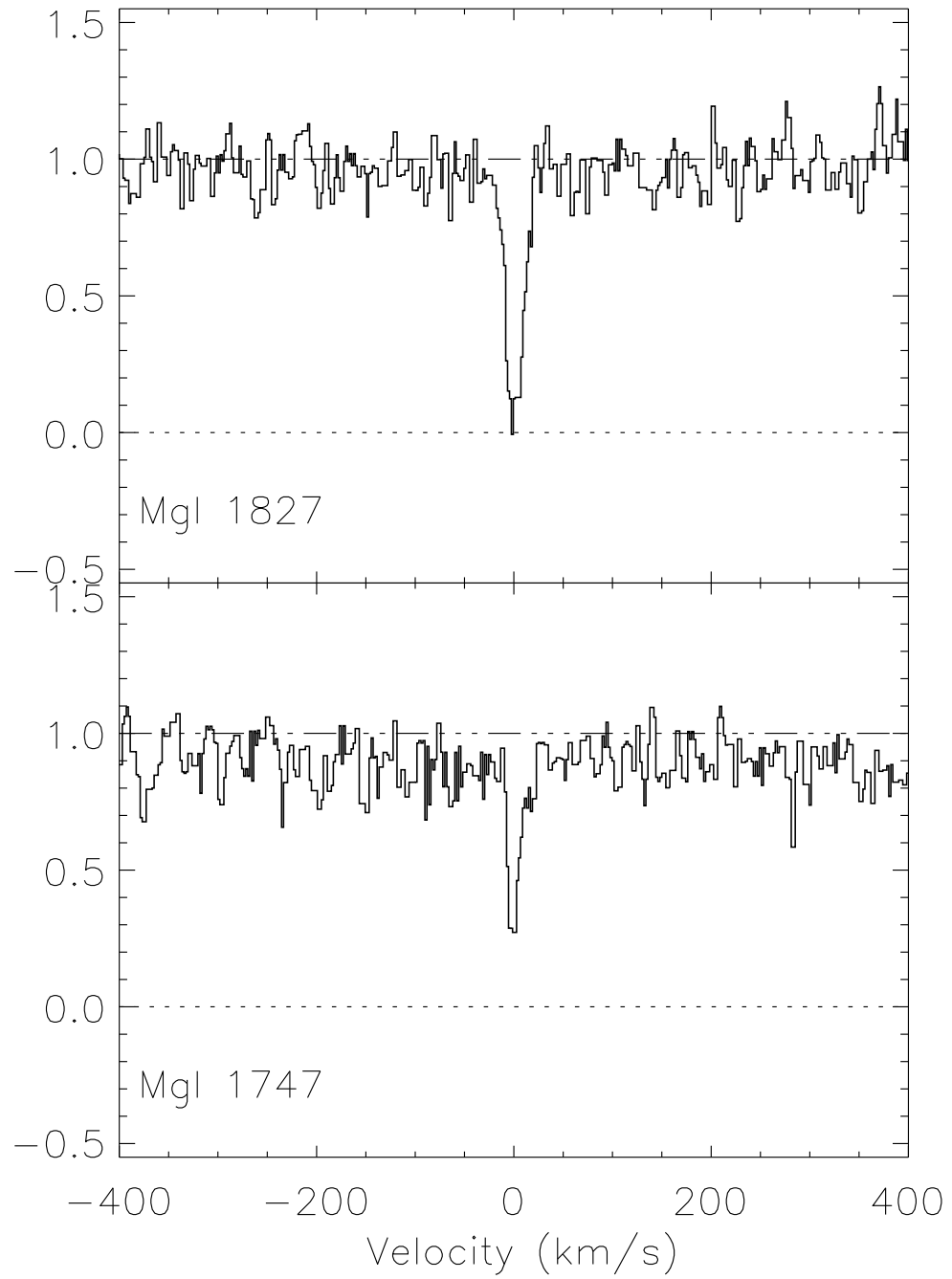


FIG. 3.— Same as Figure 2 but for Mg I transitions.

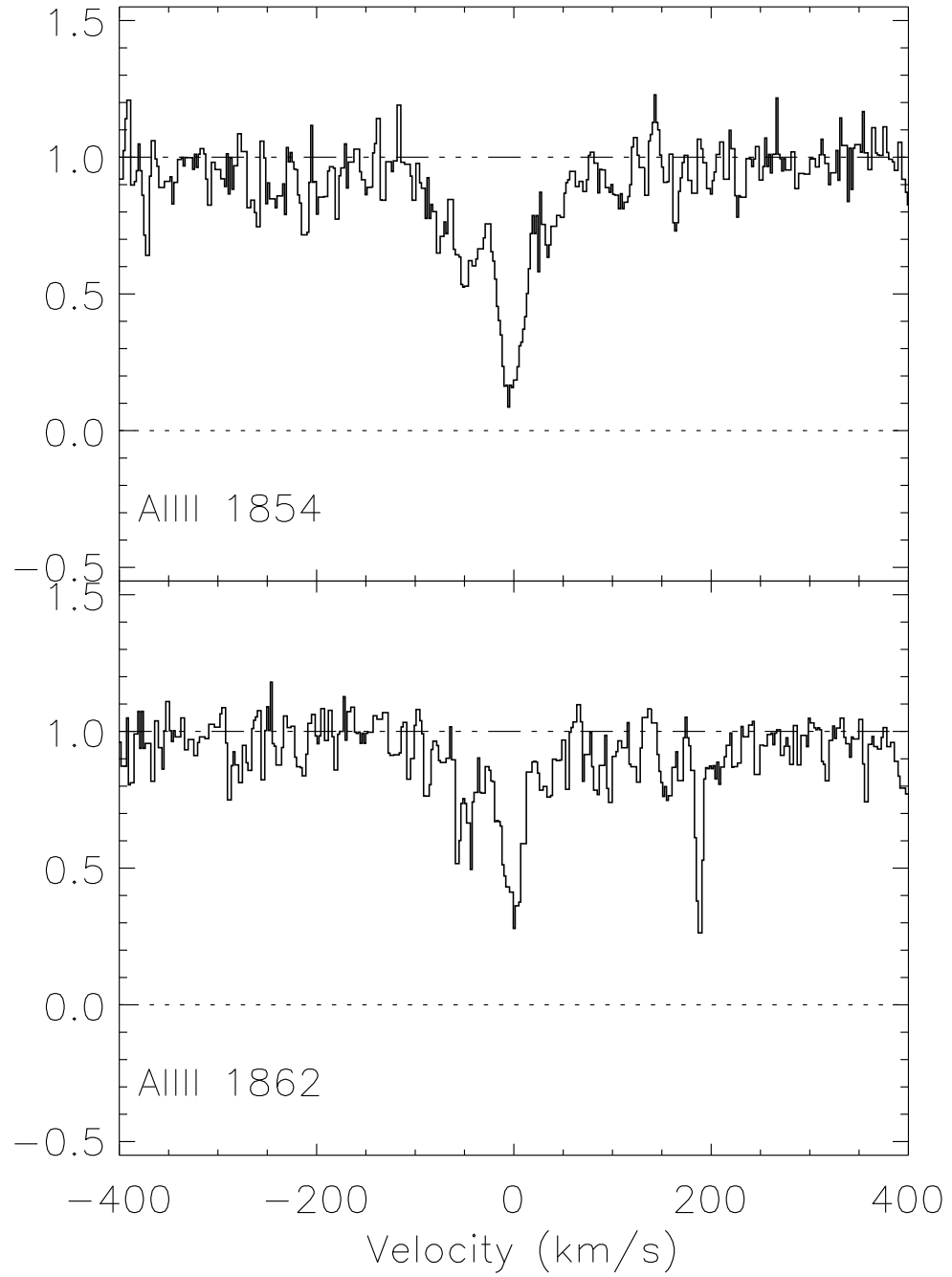


FIG. 4.— Same as Figure 2 but for Al III transitions.

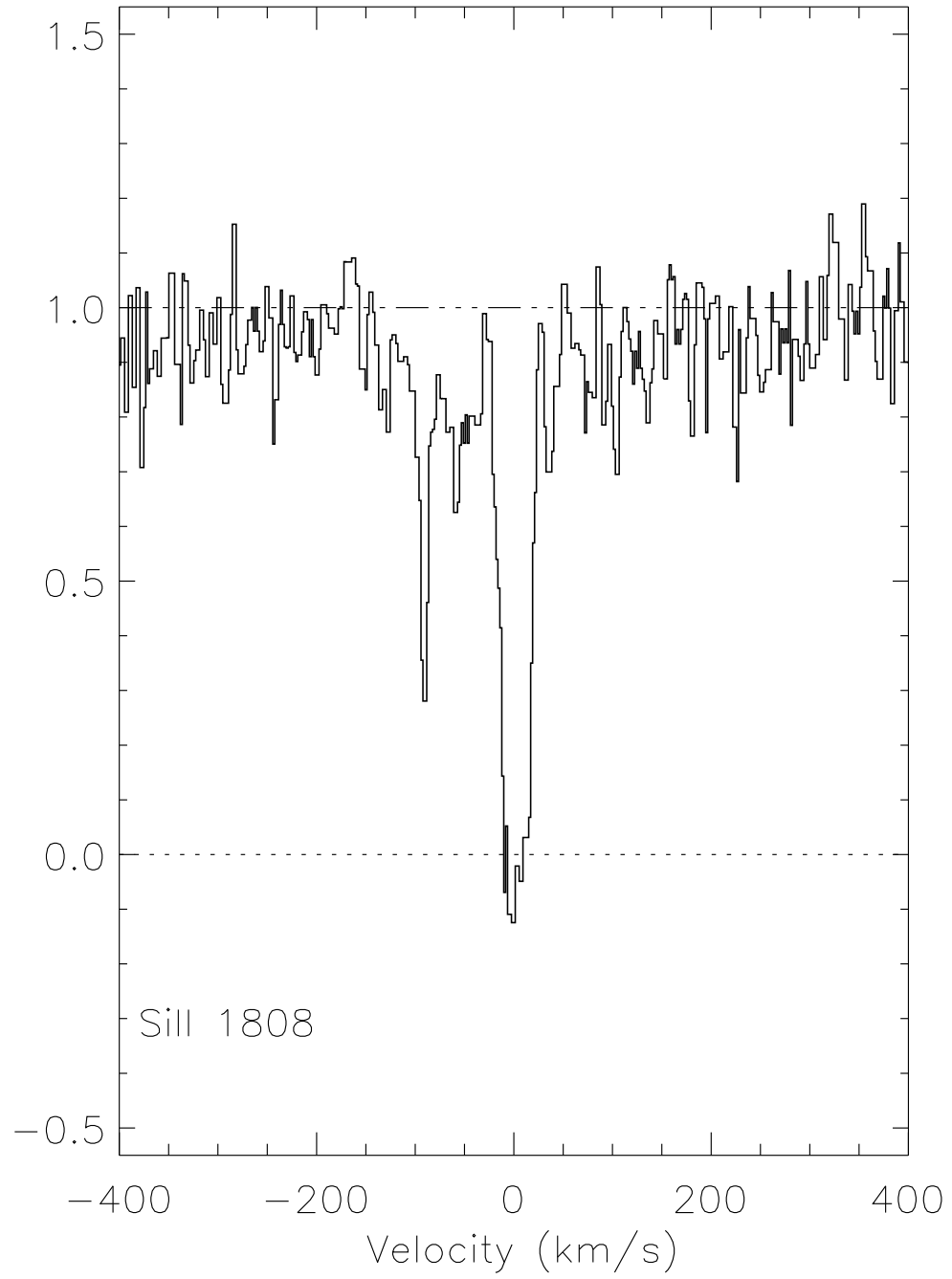


FIG. 5.— Same as Figure 2 but for Si II transitions.

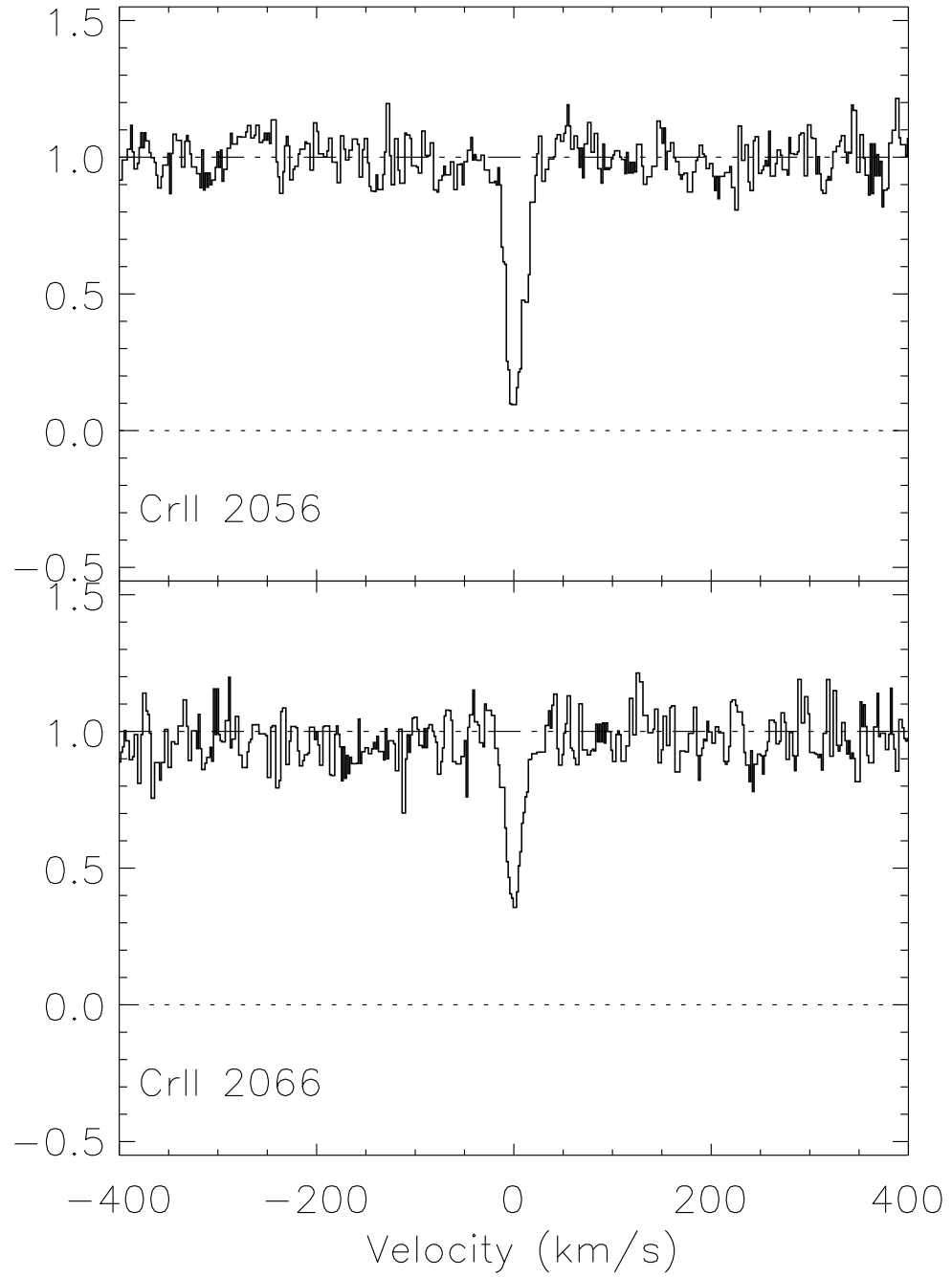


FIG. 6.— Same as Figure 2 but for Cr II transitions.

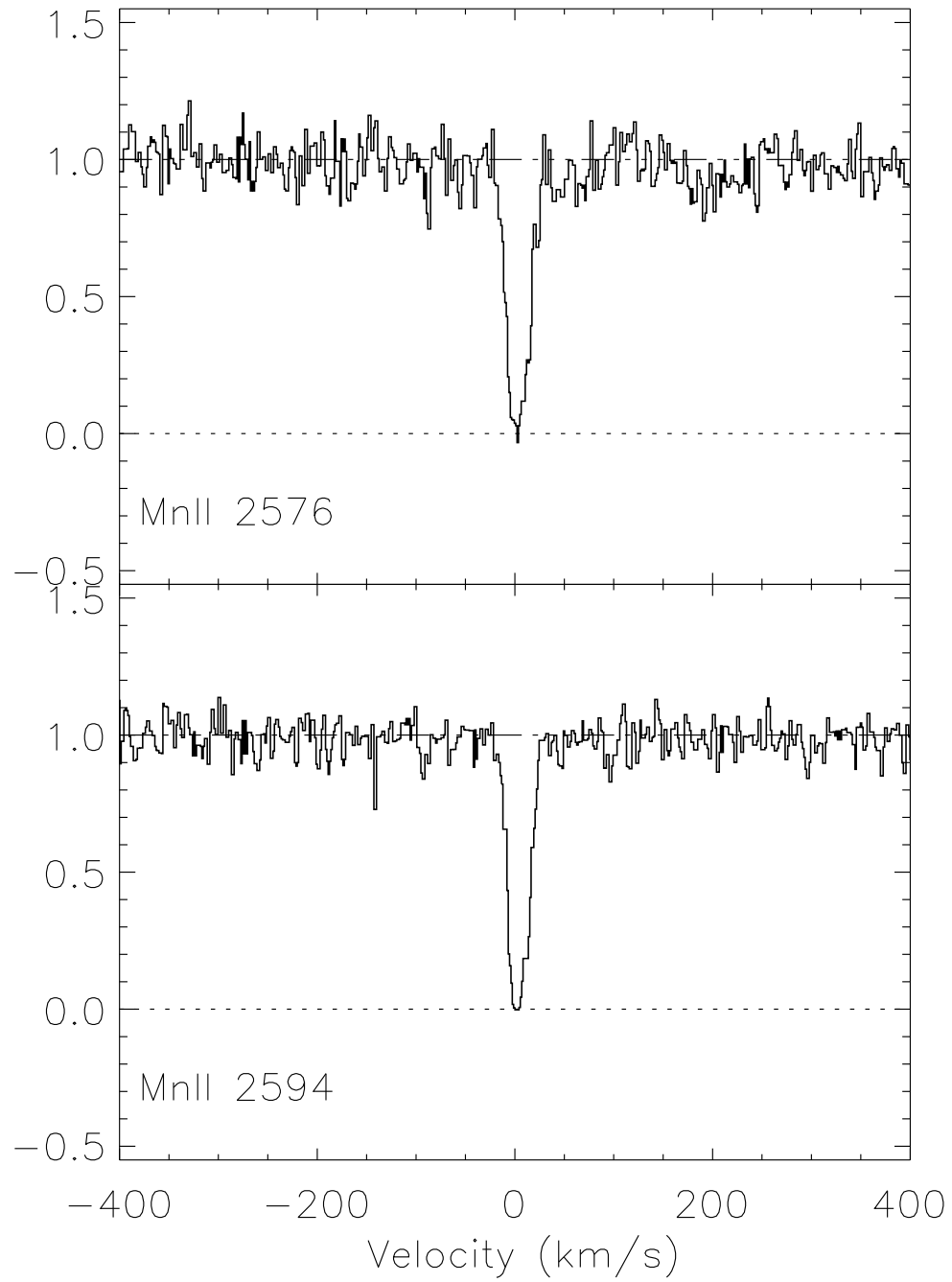


FIG. 7.— Same as Figure 2 but for Mn II transitions.

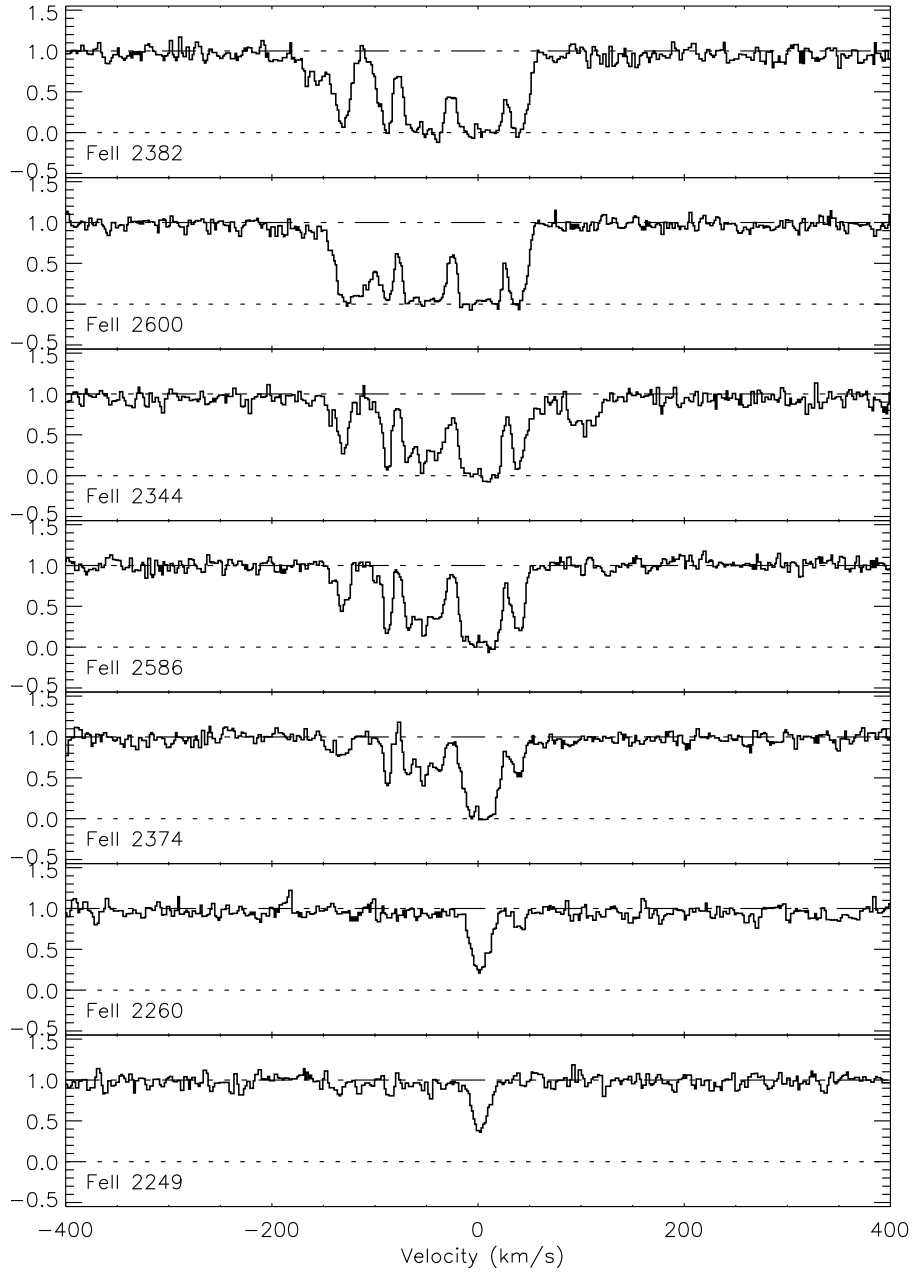


FIG. 8.— Same as Figure 2 but for Fe II transitions. The Fe II absorption has a velocity structure similar to that of Mg II, and the large number of transitions of differing oscillator strength enables recovery of the kinematics in the dense core from $-30 < v < 30 \text{ km s}^{-1}$, as well as the outlying absorption from $-200 < v < 60 \text{ km s}^{-1}$.

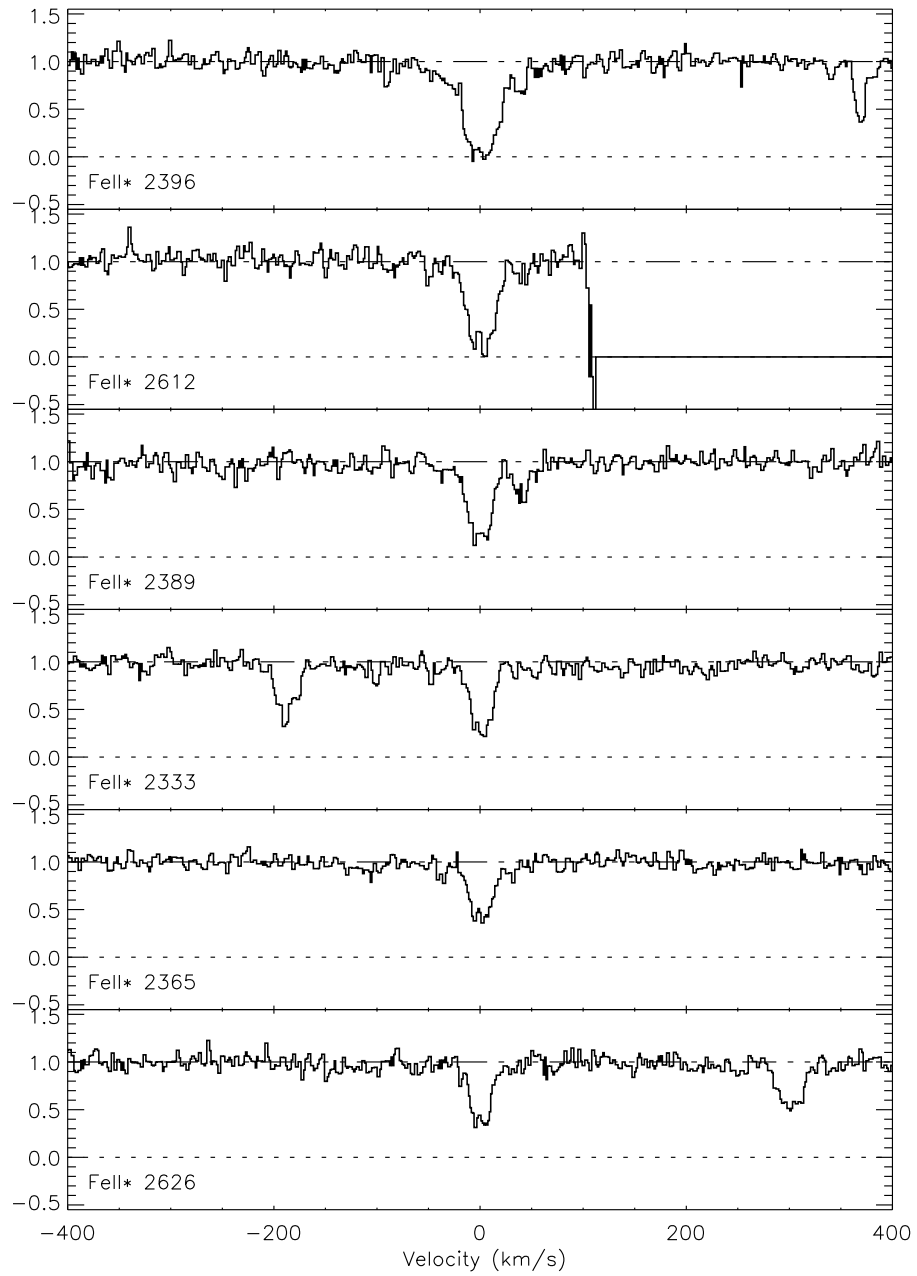


FIG. 9.— Same as Figure 2 but for Fe II* transitions.

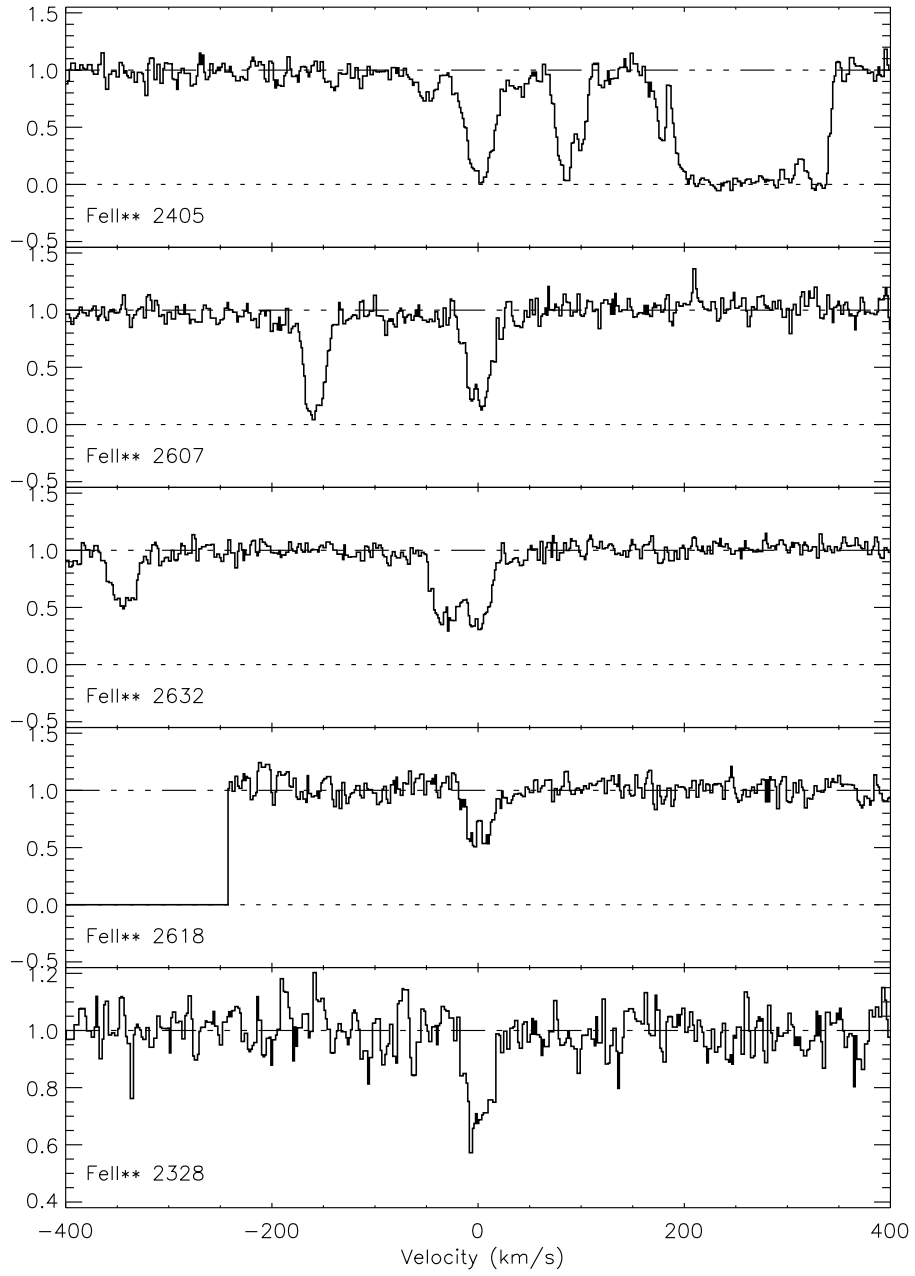


FIG. 10.— Same as Figure 2 but for Fe II** transitions.

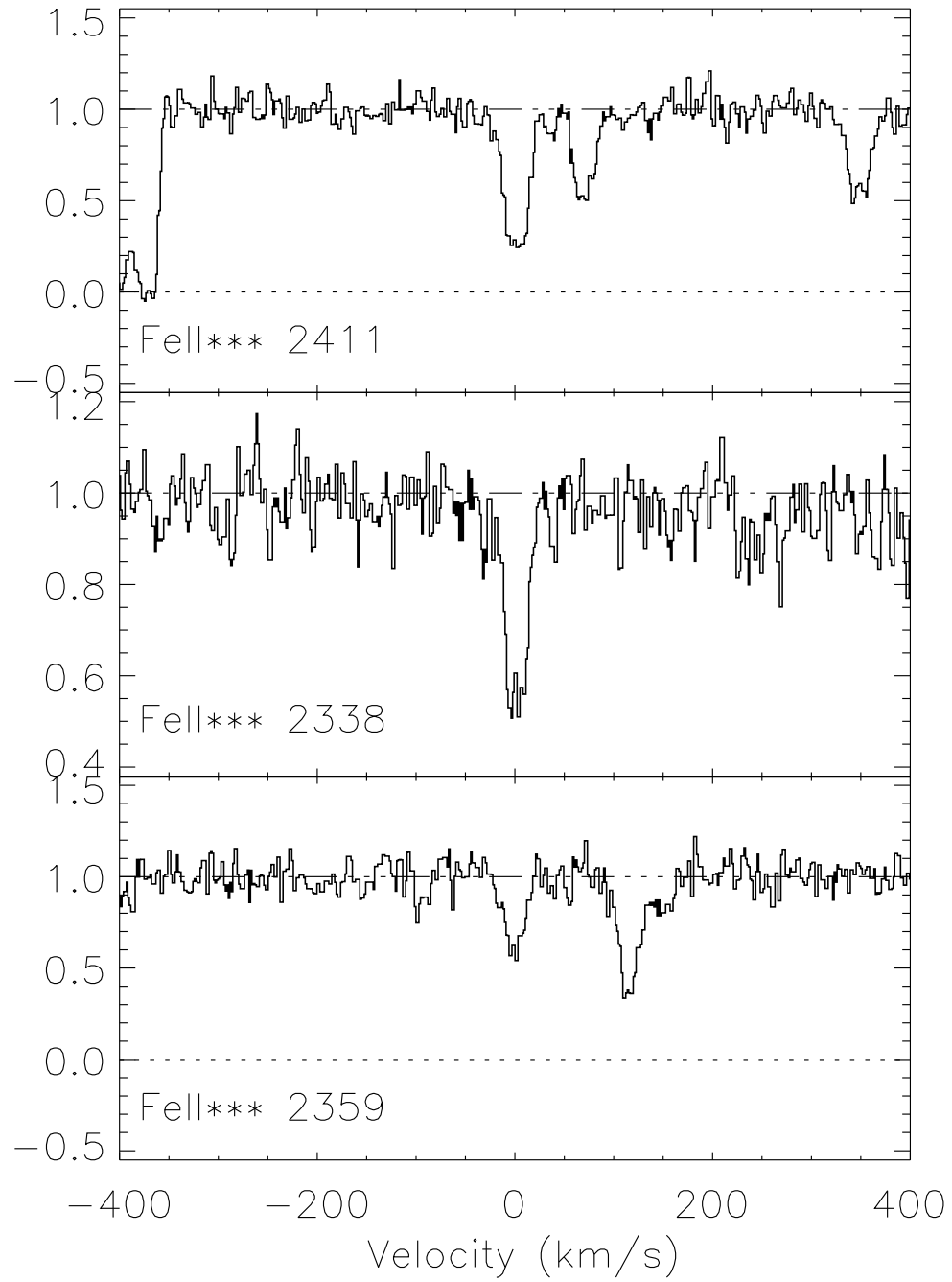


FIG. 11.— Same as Figure 2 but for Fe II*** transitions.

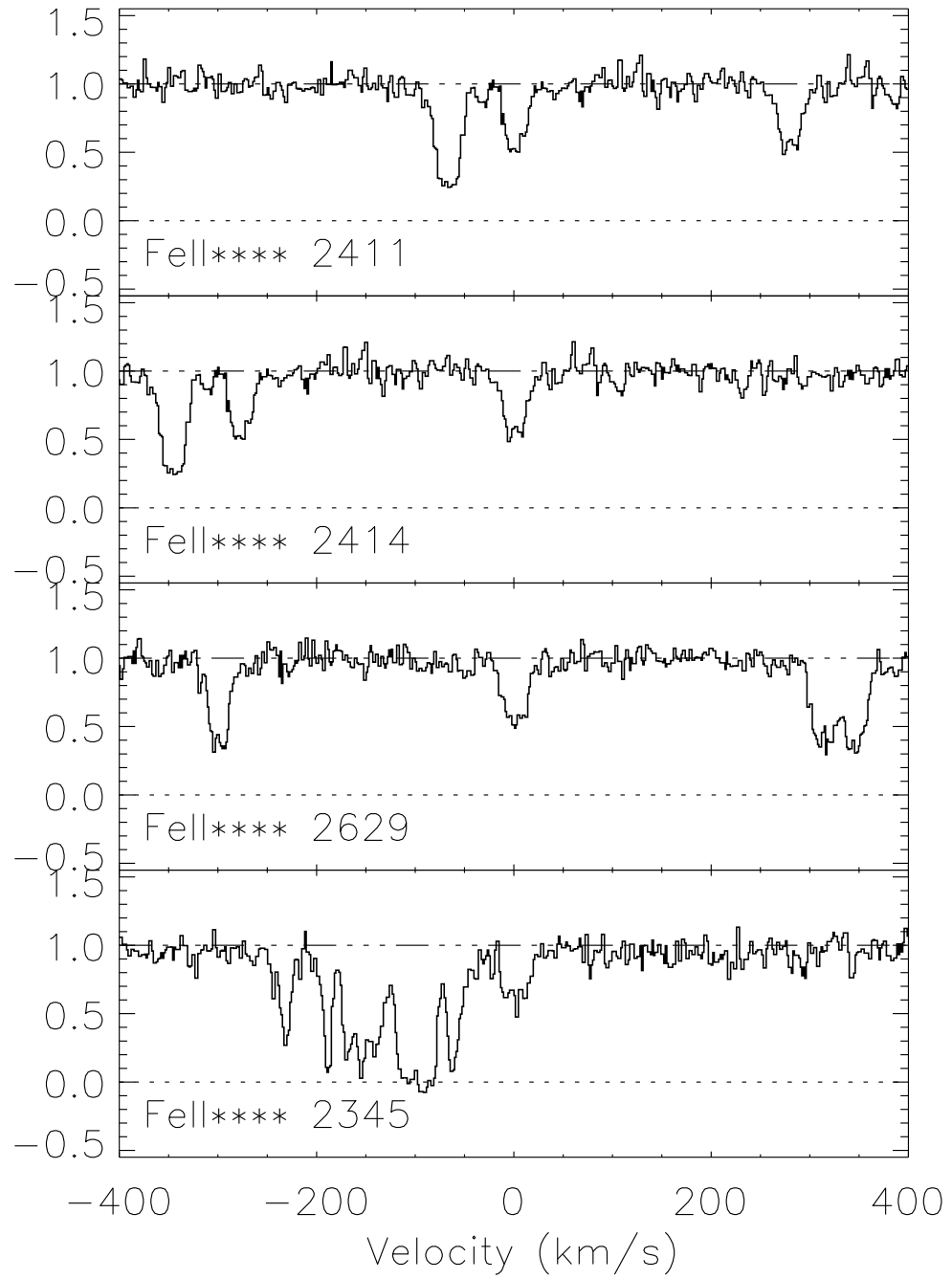


FIG. 12.— Same as Figure 2 but for Fe II**** transitions.

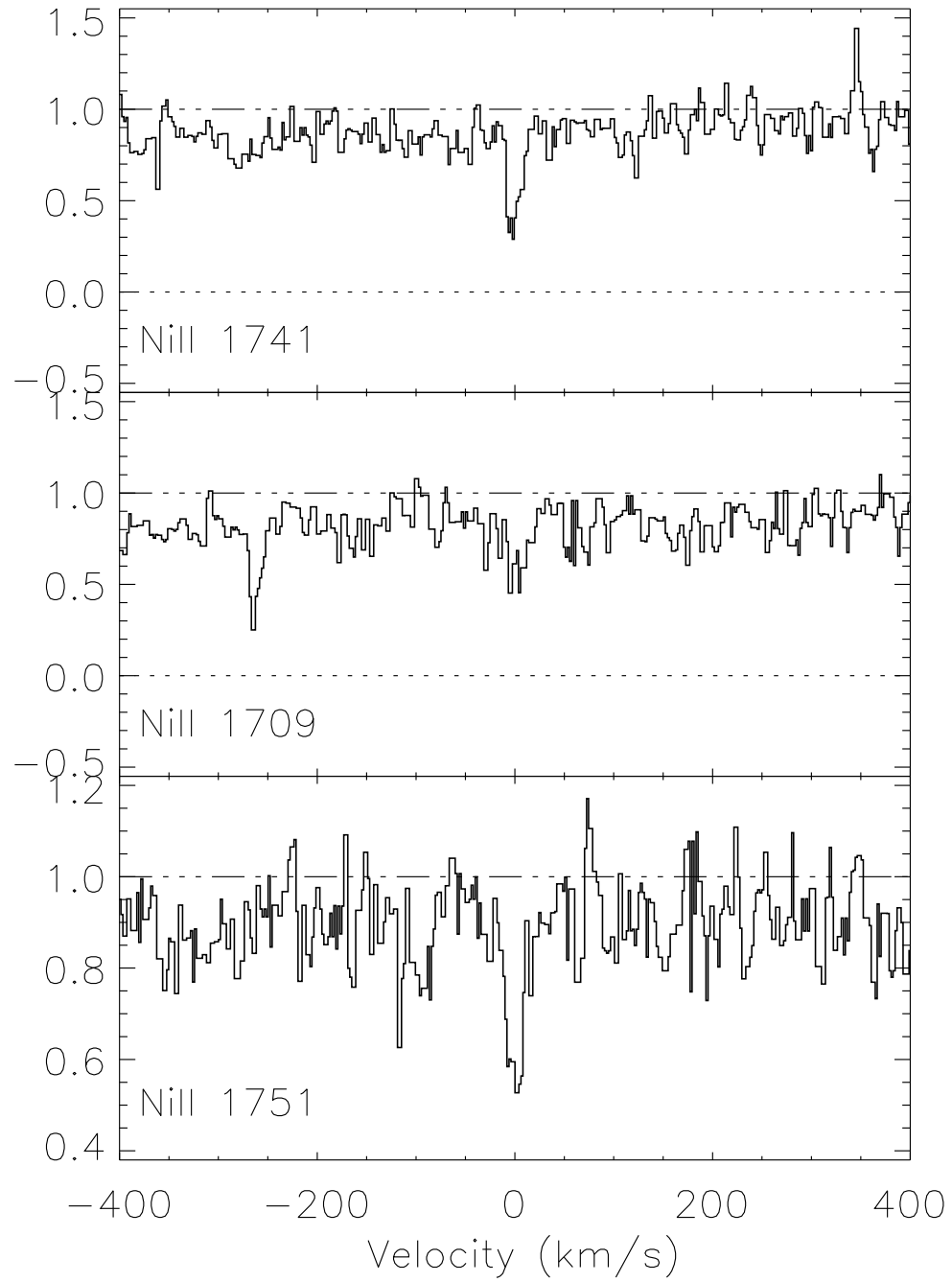


FIG. 13.— Same as Figure 2 but for Ni II transitions.

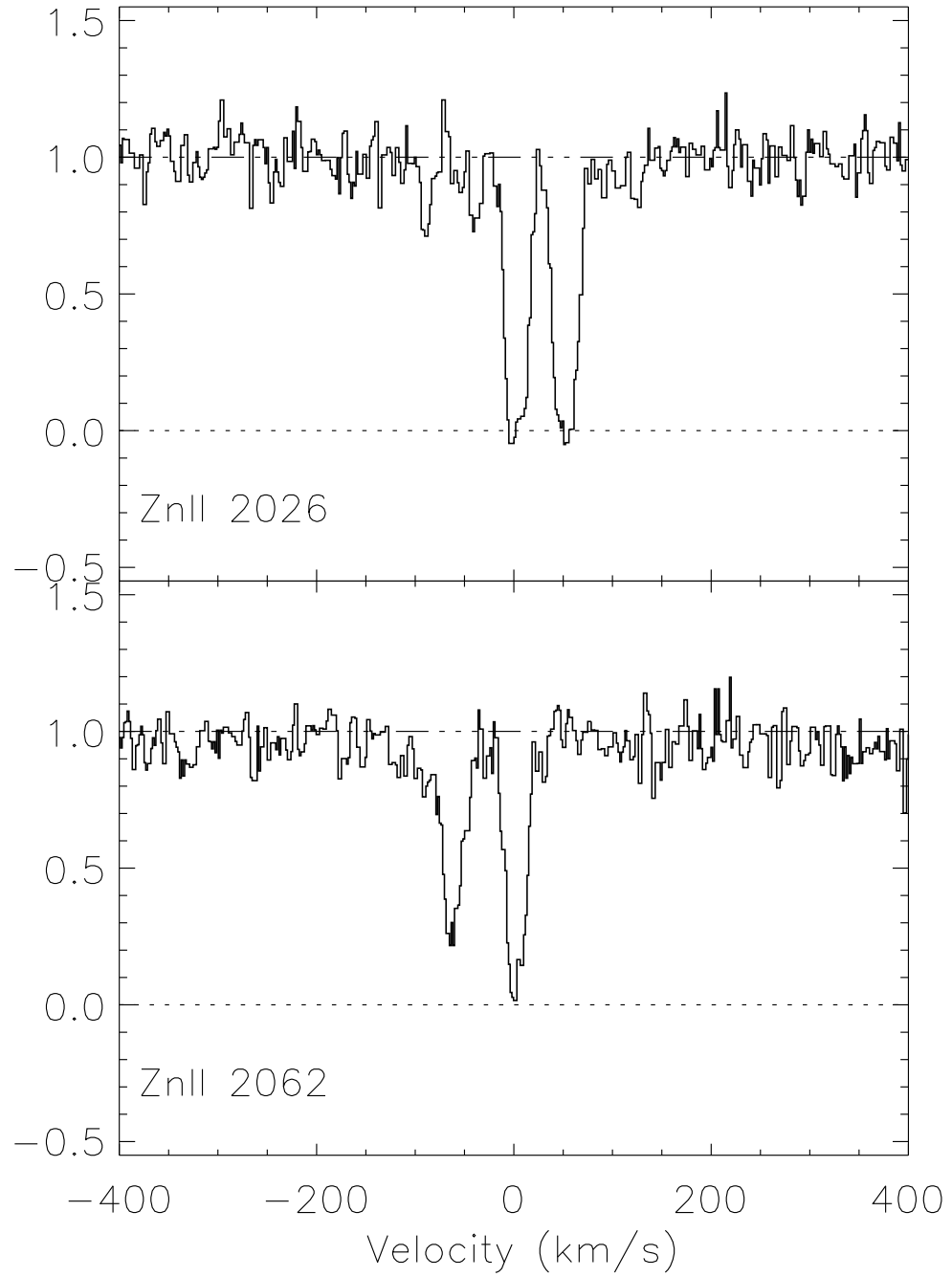


FIG. 14.— Same as Figure 2 but for Zn II transitions.

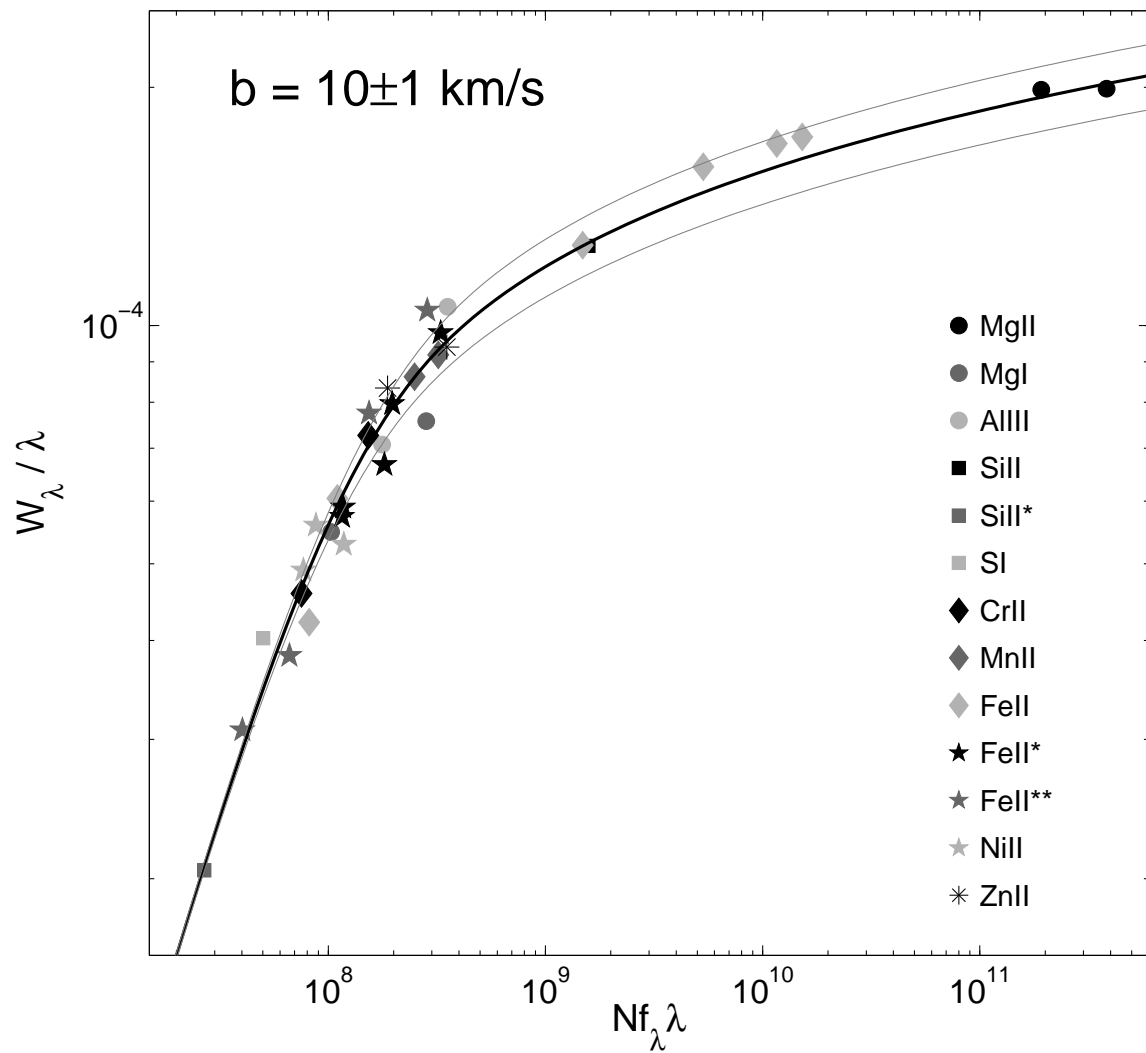


FIG. 15.— Curve of growth (COG) for the host galaxy system of GRB051111. We constructed the COG by iteratively fitting for the column densities of individual ions and for the Doppler parameter, b , which we assumed to have a single value. Transitions in the linear part of the COG lead to well-determined columns. Transitions on the flat portion of the COG are sensitive to the value of b .

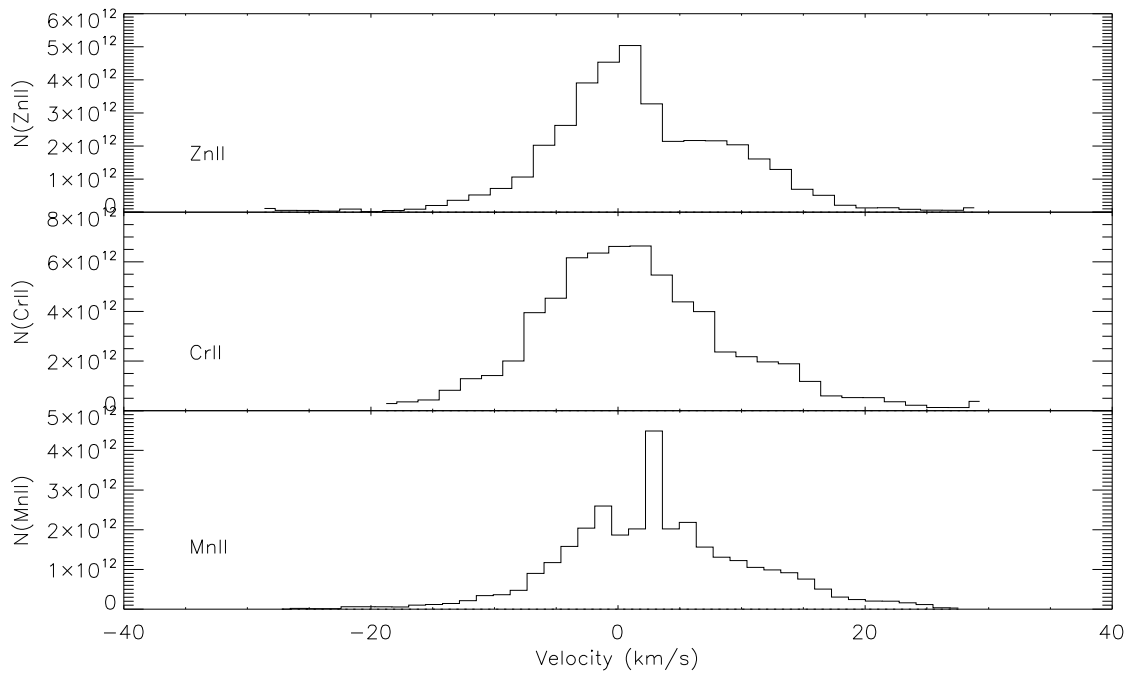


FIG. 16.— Stacked plot of $N(v)$ of the ions Zn II, Cr II, and Mn II, showing the strongly peaked, and narrow component at $-30 < v < 30 \text{ km s}^{-1}$.

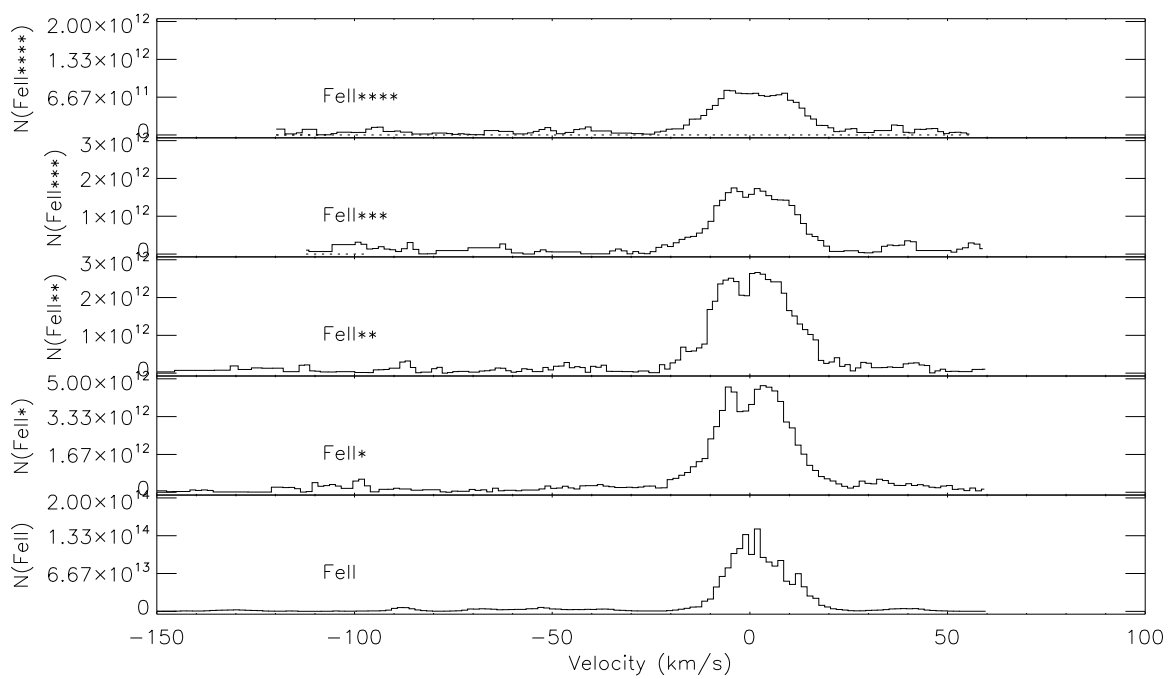


FIG. 17.— Stacked plot of $N(v)$ for the fine-structure excited Fe II levels within the main absorption system of GRB 051111, plotted across the entire velocity range of detected Fe II. The kinematics of the Fe II across the fine structure levels shows a strong and relatively narrow pair of peaks with slightly broader absorption in the higher excitation levels.

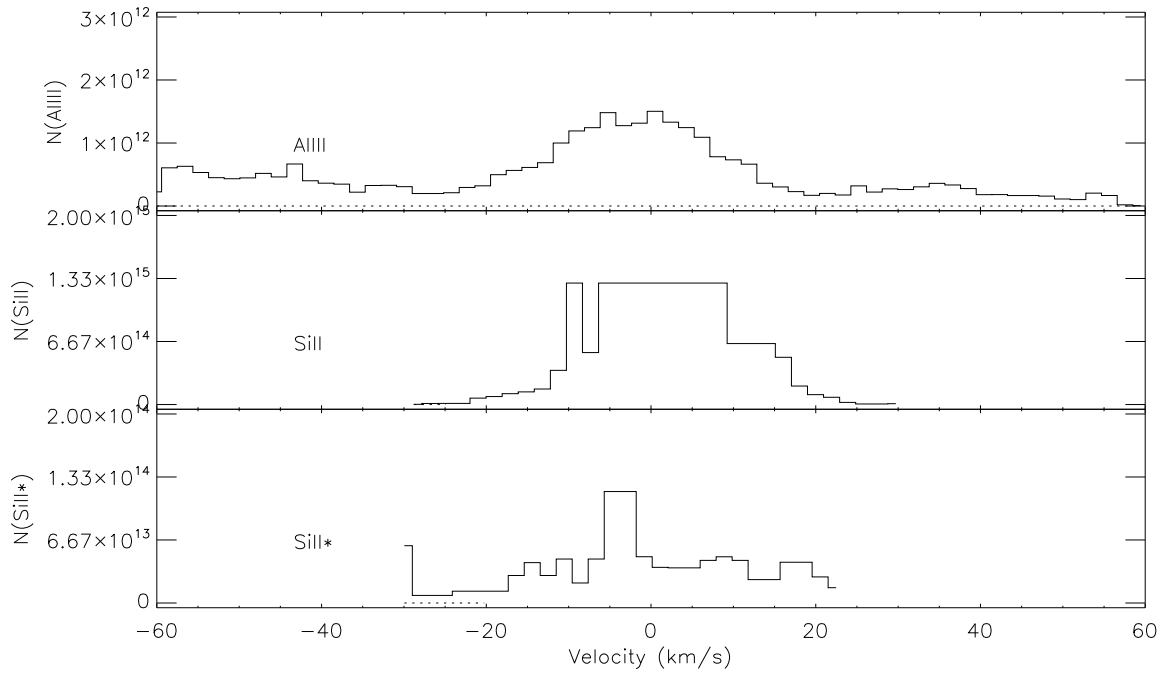


FIG. 18.— Stacked plot of $N(v)$ for the Al III, Si II and Si II* within GRB 051111. The Si II line is saturated, and our resulting column density is a lower limit. The Si II* column density is clearly much weaker compared to the ground-state than is observed in the case of Fe II.

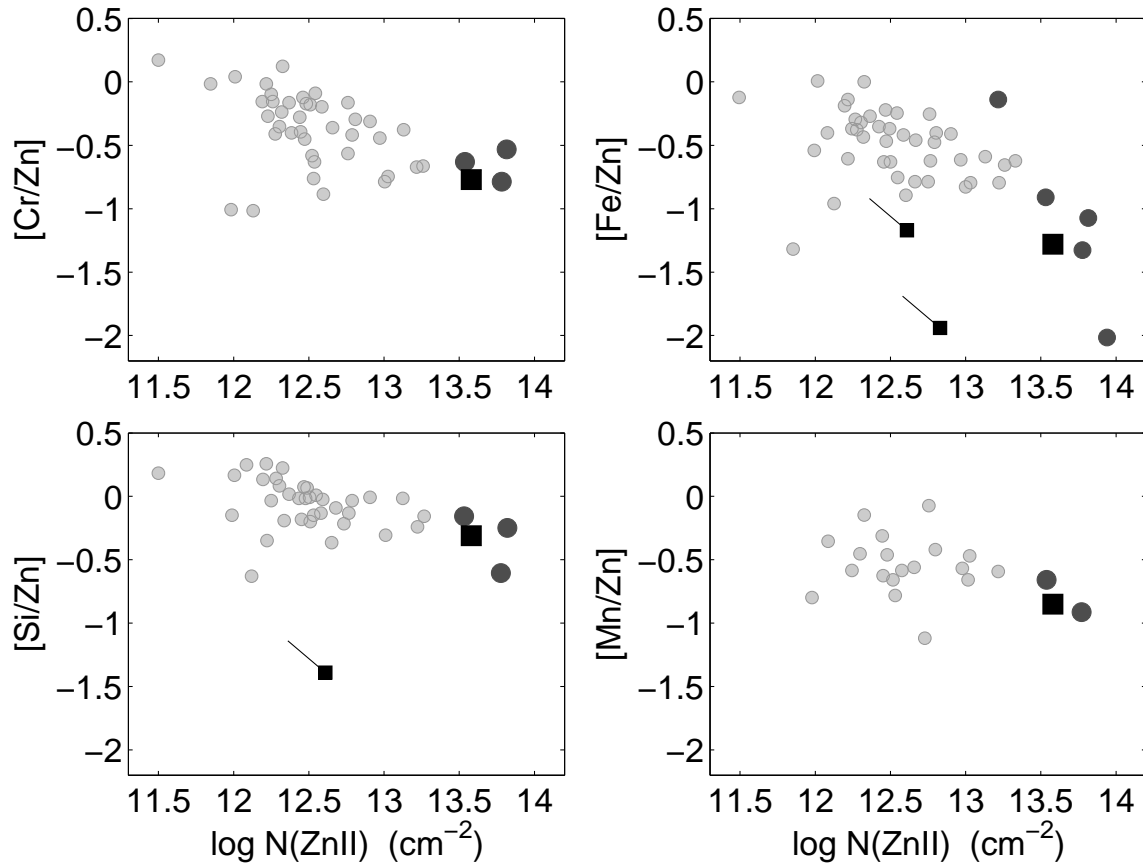


FIG. 19.— Column density ratios from GRB051111 of various species compared to the non-refractory Zn II (squares), along with the values for past GRB-DLAs and for QSO-DLAs (circles). The DLA sample is taken from (Savaglio & Fall 2004), and is consistent with a newer DLA sample from the Keck HIRES spectrograph. Small squares show the range of values possible for absorption from the system at larger velocities outside the main $-30 < v < 30 \text{ km s}^{-1}$, and where we have lower limits, the ratios follow the vector indicated in the figure.

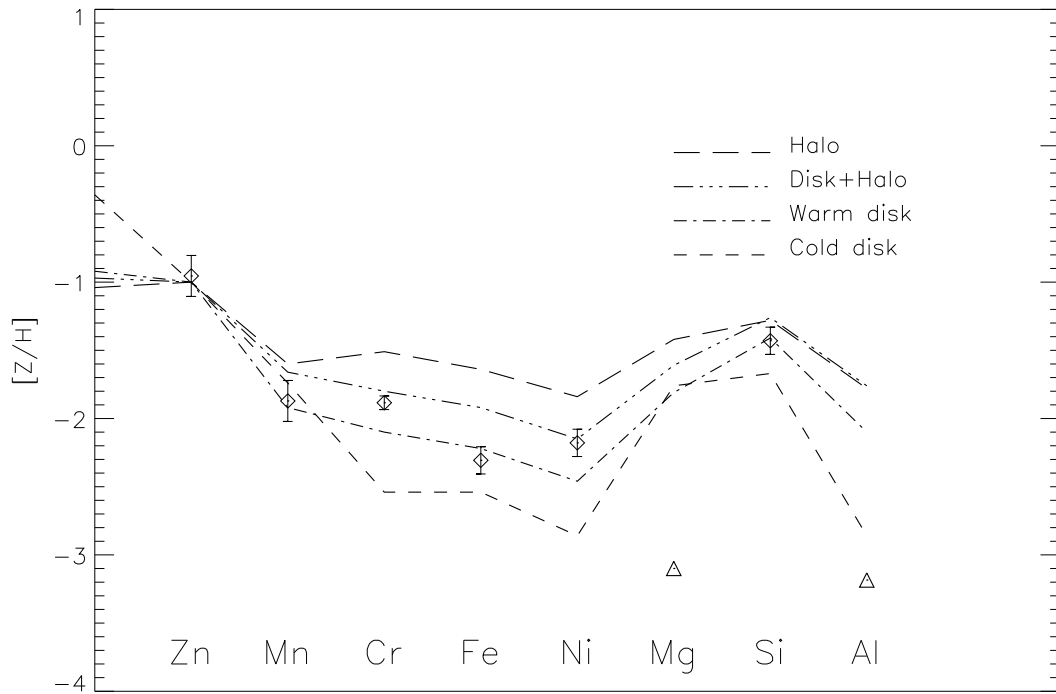


FIG. 20.— Depletion pattern for the main absorber (z_{1b}) in the host galaxy of GRB051111. The pattern of depletion is typical for warm disk clouds such as those of observed in the Milky Way (Savage & Sembach 1996).

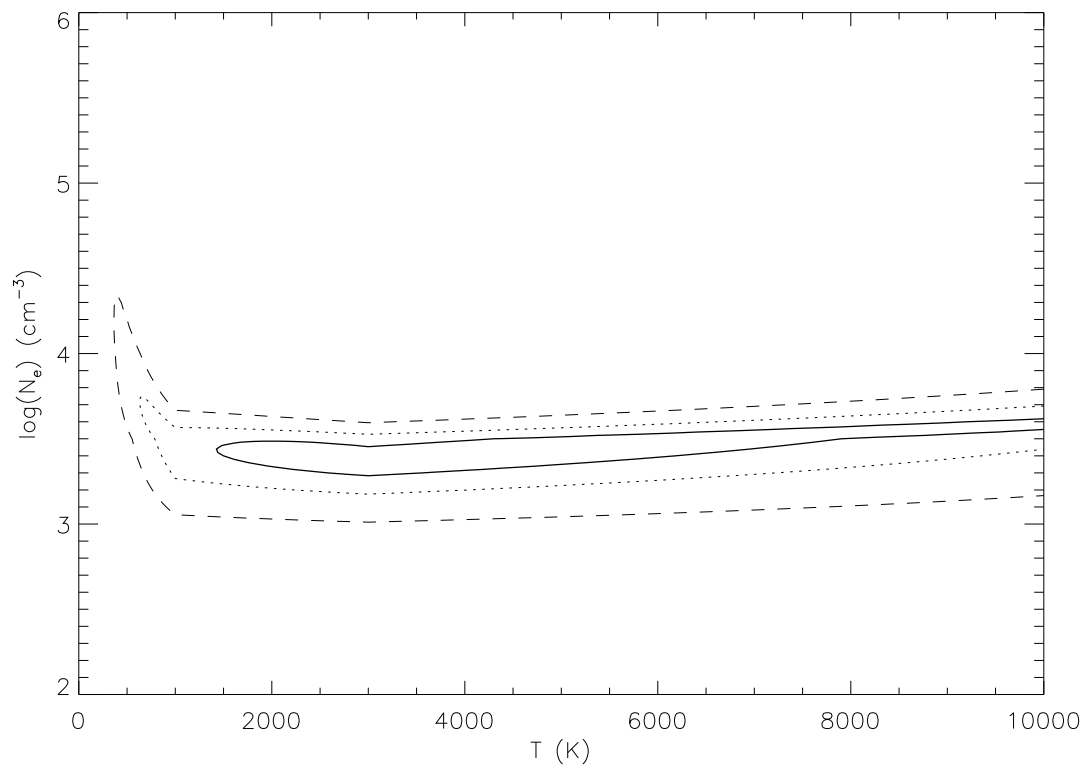


FIG. 21.— Reduced χ^2 contours for the Fe II fine-structure column densities compared to the ground-state compared with predictions from Keenan et al. (1988). The contours show values of $\chi_r^2 = 1$ (solid), 2 (dotted) and 5 (dashed), giving a range of possible density and temperature within the GRB 051111 absorber, assuming collisional excitation.

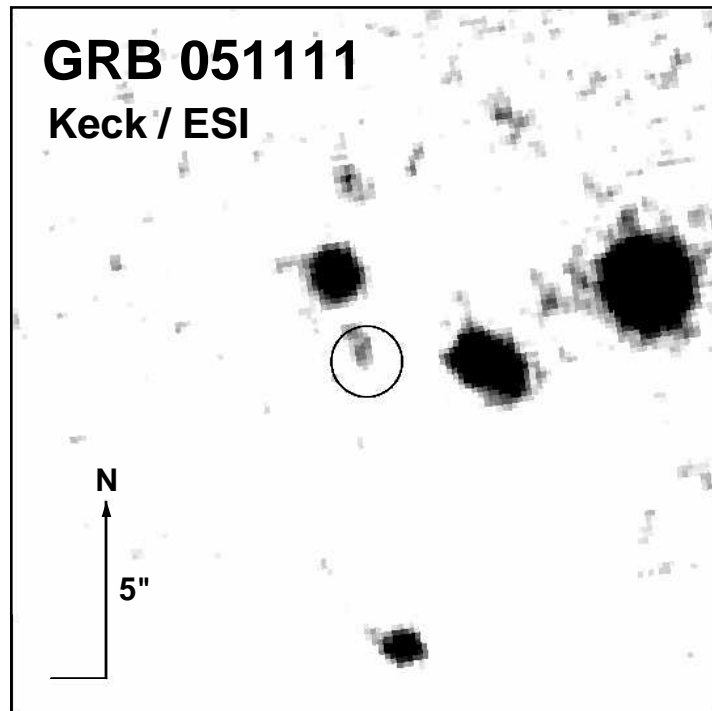


FIG. 22.— Keck ESI image of the field near GRB051111, showing the error circle of the coordinates for the GRB051111 (shown with the circle), and two adjacent galaxies probably responsible for the intervening Mg II and Fe II absorption lines seen at lower redshifts of $z_2 = 1.18975$, $z_{3a} = 0.82761$ and $z_{3b} = 0.82698$. The $2 - 3''$ offset from the centers of these adjacent galaxies amounts to a distance from the center of the galaxy of $15 - 20$ kpc.